



# A digital twin of liver predicts regeneration after drug-induced damage at the level of cell type orchestration

Jieling Zhao, Ahmed Ghallab, Reham Hassan, Steven Dooley, Jan G Hengstler, Dirk Drasdo

## ► To cite this version:

Jieling Zhao, Ahmed Ghallab, Reham Hassan, Steven Dooley, Jan G Hengstler, et al.. A digital twin of liver predicts regeneration after drug-induced damage at the level of cell type orchestration. 2022. hal-03738207

**HAL Id: hal-03738207**

**<https://inria.hal.science/hal-03738207>**

Preprint submitted on 25 Jul 2022

**HAL** is a multi-disciplinary open access archive for the deposit and dissemination of scientific research documents, whether they are published or not. The documents may come from teaching and research institutions in France or abroad, or from public or private research centers.

L'archive ouverte pluridisciplinaire **HAL**, est destinée au dépôt et à la diffusion de documents scientifiques de niveau recherche, publiés ou non, émanant des établissements d'enseignement et de recherche français ou étrangers, des laboratoires publics ou privés.

# A digital twin of liver predicts regeneration after drug-induced damage at the level of cell type orchestration

Jieling Zhao<sup>1,2</sup>, Ahmed Ghallab<sup>1,3</sup>, Reham Hassan<sup>1,3</sup>, Steven Dooley<sup>4</sup>, Jan G. Hengstler<sup>1</sup>, Dirk Drasdo<sup>1,2,\*</sup>

<sup>1</sup>Leibniz Research Centre for Working Environment and Human Factors, Technical University of Dortmund (IfADo), Dortmund, Germany; <sup>2</sup>Institut National de Recherche en Informatique et en Automatique (INRIA), Saclay, France; <sup>3</sup>Department of Forensic Medicine and Toxicology, Faculty of Veterinary Medicine, South Valley University, Qena, Egypt; <sup>4</sup>Molecular Hepatology Section, Department of Medicine II, Medical Faculty Mannheim, Heidelberg University, Mannheim, Germany

\*Correspondance: dirk.drasdo@inria.fr (D.D.)

## ABSTRACT

This communication presents a mathematical mechanism-based model of the regenerating liver after drug-induced pericentral lobule damage resolving tissue microarchitecture. The consequence of alternative hypotheses about the interplay of different cell types on regeneration were simulated. Regeneration dynamics has been quantified by the size of the damage-induced dead cell area, the hepatocyte density and the spatial-temporal profile of the different cell types. We use deviations of observed trajectories from simulated system to identify branching points, at which the systems behavior cannot be explained by the underlying set of hypotheses anymore. Our procedure reflects a successful strategy for generating a fully digital liver-twin that, among others, permits to test perturbations from the molecular up to the tissue scale. The model simulations are complementing current knowledge on liver regeneration by identifying gaps in mechanistic relationships and guiding the system towards the most informative (lacking) parameters that can be experimentally addressed.

## KEYWORDS

Digital liver twin; Liver regeneration; Agent-based model; Liver lobule; DILI; Tissue micro-architecture; Cell types; Cell-cell signaling

## INTRODUCTION

The liver is the main detoxifying organ in the human body to remove drugs and toxins from the blood. It is organized in 2-5 lobes (depending on the species), which itself are composed of hexagonal-shaped repetitive histological and functional units, called lobules. Oxygen-rich blood transported via the hepatic artery from the aorta and oxygen-poor blood carried via the portal veins from the intestine mix up in the periphery of the lobule, perfuse it through a network of fenestrated capillaries (called sinusoids) and then drain into the "central vein" (CV).

Administration of a hepatotoxic dose of protein alkylating compounds, e.g., acetaminophen (Paracetamol, APAP, 300 mg/kg, i.p. in mouse), or carbon tetrachloride (CCl<sub>4</sub>, 1 g/kg, i.p. in mouse), generate a pericentral damage of about 50% of the hepatocytes in the lobule that is subsequently in most cases perfectly regenerated, both histologically and functionally (Zieve et al., 1985, Hoehme et al., 2007, 2010, Ghallab et al., 2016). APAP is the most frequent cause for acute liver failure (Olson et al., 2017) and a "model substance" to study drug-induced acute liver injury and its adverse outcome on cells, organs, and organisms through a series of successive key events, recently discussed in detail in the context of the popular concept of Adverse Outcome Pathways (AOPs) (Leist et al., 2017).

CCl<sub>4</sub> is a frequently studied hepatotoxic compound using a different detoxification pathway but generating a very similar spatial-temporal liver tissue damage pattern and downstream regeneration response. Several mechanisms may contribute to the death of hepatocytes. Cytochrome P450-enzymes such as Cyp2e1 and Cyp1a2 (summarized in this work as CYP450) metabolize APAP (or CCl<sub>4</sub>) into toxic radicals, which downstream causes oxidative stress, dysfunction of mitochondria, and DNA damage, resulting in mitochondrial membrane permeability transition and hepatocyte death. In addition to these initiation events, inflammatory mediators such as bile acids, cytokines and chemokines, the latter two predominantly secreted by non-parenchymal and immune cells, may critically contribute in the APAP-induced liver injury (Liu et al., 2004, Ghallab et al., 2022).

Upon repetitive administration, both compounds generate liver fibrosis, which has led to a wide use of both compounds to study the development of chronic liver disease in rodent models (O'dell et al., 1986, Ghallab et al., 2019, Nevzorova et al., 2020). Chronic liver disease is a consequence of compromised regeneration that is incapable of repairing repetitive tissue injury. Understanding the mechanisms controlling regeneration is a major subject of investigation in order to improve treatment of chronic liver disease and regeneration after acute liver injury, including partial hepatectomy.

Liver regeneration is an overly complex process involving many different cell types and factors (Kang et al., 2012, Kisseleva and Brenner, 2021, Michalopoulos and Bhushan, 2021). Upon inflicted liver damage, the injured main hepatic parenchyma cells, namely, hepatocytes start to release factors to trigger an inflammatory response (Calderwood et al., 2016, Li et al., 2020). Liver resident macrophages, namely, Kupffer cells are activated to recruit neutrophils to initiate death of injured hepatocytes (Marra and Tacke, 2014). After liver injury is initiated, hepatic stellate cells (HSCs) migrate into the lesion and become activated through stimulating factors released from damaged hepatocytes, the activated macrophages, the extracellular matrix, neighboring sinusoidal endothelial cells and platelets (Puche et al., 2013, Michalopoulos and Bhushan, 2021). After the liver injury, there is also massive infiltration of bone marrow derived (non-resident) macrophages into the liver to elicit liver impairment and to restore liver integrity at different stages (Tacke and Zimmermann, 2014). Despite extensive studies over decades, the precise orchestration is only partially understood, and the understanding is mainly qualitative.

There are alternative sets of hypotheses on how certain factors interplay, and it is not well understood how sensitive the regeneration outcome is regarding a modification of time scales or rate constants. This is difficult to study experimentally for several reasons: (1) the primary motivation for experiments is to understand the regeneration process in human, but experiments in human are per se not permitted and experiments in animal models are subject to close ethical control and do not fully reflect the processes in human; (2) the rate constants and time scales are generally hard to control in animal experiments; and (3) the experiments are resource-intense with regards to personnel, technology, animal numbers and consumables. Hence, a promising strategy may be to formulate alternative sets of mechanisms and implement them on the computer within a virtual liver twin. The consequences of these mechanisms on the regeneration process can be simulated and the most promising perturbations or facilitations proposed for "wet-lab" approval. Such strategy establishes computational model-guided experimentation by identifying the most informative experiment regarding a certain scientific question and can thus accelerate knowledge gain in (patho)physiological processes at all integrated levels (molecular, cellular, tissue, organ, system/body). In the discussed liver twin model, relevance and variability of the interplay of the different factors hypothesized to control liver regeneration after acute damage can be simulated and the outcome can be evaluated. Moreover, the prospective sensitivity of readout parameters of interest can be tested in silico. Theoretical variation of parameters and variables in the model can help to identify those with the largest influence on the observables.

In this study, we present a pipeline how multi-level computational modeling may inform experimental strategies to investigate liver regeneration upon toxin-induced acute injury. In the past decades, computational modeling has become more and more important to investigate the possible consequences of complex biological systems interactions from sub-cellular level to tissue level (Knutsdottir et al., 2017, Talman et al., 2019) and integrating molecular signals and mechanical interactions of cells (Thurley et al., 2015, Park et al., 2017, Kim et al., 2018, Stepanova et al., 2021), or directly address the mechanical contributions to biological observed phenomena in multicellular populations (Vishwakarma et al., 2018, Schwarz, 2020). This emerges as the complexity of the possible interactions makes it difficult to infer the consequences of certain mechanisms or perturbations by reasoning alone; in the meantime, even the computational multicellular models call for sophisticated methods of parameter inference (Jagiella et al., 2017). There are many computational studies developed to explore the underlying mechanisms of liver regeneration and disease processes (e.g. Drasdo et al., 2014 and refs therein). Ordinary differential equations were used to describe the dynamics of molecular factors to regulate the distinct functional states of hepatocytes in response to partial hepatectomy (Verma et al., 2019) and to reproduce the patterns of acute drug-induced toxicity (Kuepfer et al., 2018). Models based on set of partial differential equations were developed to mimic the behavior of glucose regulation in liver with diabetes (Hetherington et al., 2012), to investigate the function-perfusion processes of liver cancer (Lambers et al., 2021), and to simulate the drug perfusion in the liver (Schwen et al., 2014, 2016). Friedman and Hao (2017)

built a system of partial differential equations representing the network of liver fibrosis to explore the efficacy of potential drugs to block the fibrosis progression. Jerby et al. (2010) constructed a generic model based on network of various molecular data sources for human liver metabolism. Remien et al. (2012) used nonlinear ordinary differential equations to study the liver dysfunction. Wambaugh and Shah (2010) used an agent-based hepatic model integrating a graphical model of the sinusoidal network to study the chemical metabolization in the liver. Dutta-Moscato et al. (2014) used an agent-based model to study the liver inflammation and fibrosis. Ho et al. (2020, 2020a) constructed an *in-silico* pipeline integrating hepatic vessels and blood flow for liver surgical plan. Naik et al. (2014) constructed a multi-level model integrating multiple body compartments to investigate hepatic metabolism and its associated deregulations.

We constructed a network describing the intercellular relationship between the major cell types and the biochemical signals in the process of liver regeneration from literature. We embedded this network into our spatial-temporal lobule model and tested the reference case (the normal regeneration process) and different types of perturbations, especially such that are difficult to perform experimentally. Furthermore, we ran perturbation simulations to predict the influence of cell type depletion on liver regeneration. Our model resolves liver microarchitecture, representing each cell individually as a basic modeling element with realistic cell-biomechanics. By comparison with experimental readout parameters, we were able to identify hypotheses that were incompatible with data, and which perturbation experiments critically modify the regeneration process (schematized in Fig. 5).

Our model approach presented below hence points towards getting mechanistic insight in liver damage and regeneration with less resources i.e., faster, easier and cheaper, by a simulation step prior to the experiment. The first step could be running simulations with our model that permits identifying whether a certain hypothesized mechanism (that may also be a finding from an *in vitro* experiment) would be expected to explain a certain observation *in vivo*, and/or, whether, dropping (knocking down) this mechanism is expected to change the result. In our work, the “observation” is the successful tissue regeneration compared to its failure. In case of a result change upon knock-out, a corresponding validation experiment *in vivo* may be up-prioritized while in the opposite case (no change expected) it may be dropped. In border-line cases, where either a change or no change is both possible, depending on parameters, the simulations inform about the combinations of parameters at which a change of result is expected. This contributes to turn qualitative descriptions increasingly into quantitative process information including parameterization of each component process, even in such complex situations as tissue regeneration (or degeneration). In order to optimally perform these different functions, guiding experiments, identification of experimental parameters etc., the model needs to be as realistic and quantitative as possible in its key elements, such as representation of tissue architecture, cell biomechanics, and cell-cell interaction, which guided our model choice.

We demonstrate this in the discussion section along with hypotheses made in refs. (Krenkel et al., 2014, Marques et al., 2012, Seki et al., 2007, Boulter et al., 2012).

Our modeling strategy is also able to guide diagnosis and therapy, if fed with the proper patient data. In so far, our work addresses systems complexity (Steven Hawking: "*I think the next century will be the century of complexity*").

## RESULTS

### Modeling approach

#### **Construction of a lobule: Geometry of lobule, choice of cell types, number and distribution.**

The chosen tissue unit in this work is the individual hepatic lobule. Following previous work (Fig. 1B, Hoehme et al., 2010), modeling was performed in a statistically representative lobule of hexagonal shape, with the central vein in the center of the lobule and portal veins in three of its 6 corners. The precise micro-architecture of the lobule was constructed from parameter distributions obtained from 3D liver tissue reconstructions. Upon injection of a hepatotoxin, such as CCl<sub>4</sub> (or APAP), the liver parenchymal cells, namely hepatocytes, in the pericentral region of the lobule die, resulting in a pericentral dead cell area. The starting state of the simulation was defined by labeling pericentral hepatocytes as injured and potential candidates to die. According to the current understanding of hepatotoxicity upon CCl<sub>4</sub> or APAP, the injured hepatocytes are those that are cytochrome P450-enzymes positive and received a critical dose of CCl<sub>4</sub> (or APAP) (Sezgin et al., 2018, Ghallab et al., 2021).

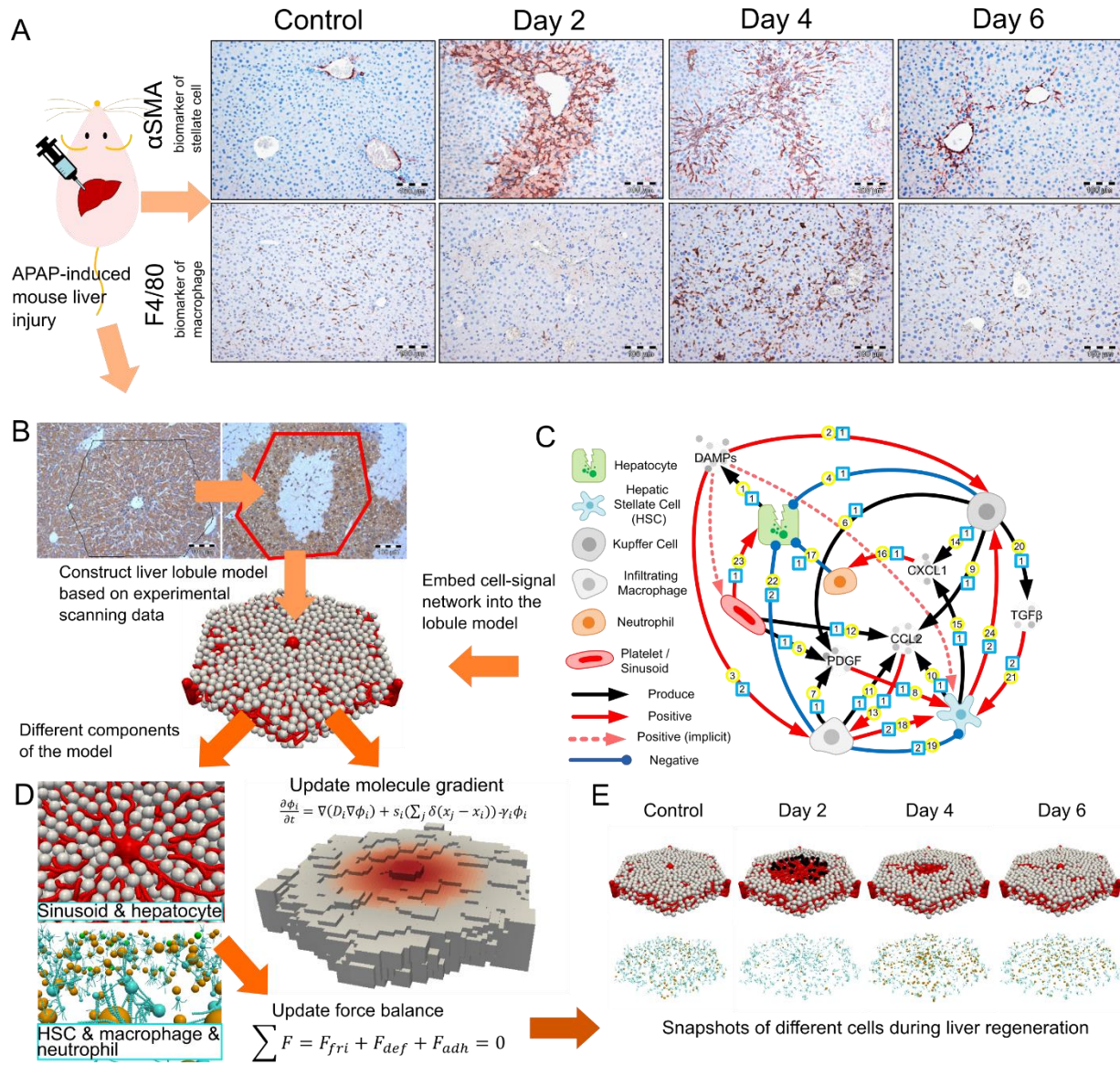


**Figure 1. Model of multi-cellular lobule system based on experiments.** (A) APAP-induced liver regeneration on mouse and the spatio-temporal pattern of the different liver cell types. We have corresponding experimental stainings as reference. (B) A lobule in hexagonal shape is constructed to study the liver regeneration process upon toxin-induced acute damage following our previous work (Hoehme et al., 2010). In this study, CCl<sub>4</sub> is used to induce lobular damage, where the necrotic lesion size reaches the maximum area 2 days after the injection of CCl<sub>4</sub>. (C) The network includes relevant cell types and intercellular signals contributing to liver regeneration. “Positive” means to activate or to attract a certain type of cell; “Negative” means to kill, to eliminate, or to deactivate a certain type of cell. The number in the yellow circle marks the related reference (Table S2). The number in the cyan square indicates its classification, (cl-)“1” indicates the relationship has literature support; (cl-)“2” indicates the relationship is discussed as option by literature without data-based evidence. (D) For the different liver cell types, specific geometric objects are used to represent their shape (grey: hepatocytes; red: sinusoids; cyan: HSCs; brown:

macrophages; green: neutrophils). Cell movement is updated by solving a force-velocity equation according to the respective cell-mechanical properties. The signal gradient is updated by solving a related diffusion equation. (E) Illustration of different cell types at different days after the injury.

## **Identification of relevant cell types and cell-cell-interaction network**

In a next step, relevant cell types were identified and incorporated in the lobule. These comprise hepatocytes, sinusoidal endothelial cells organizing the sinusoidal network, hepatic stellate cells (HSCs), macrophages (both Kupffer cells and infiltrating macrophages), platelets, and neutrophils (Fig. 1C). Two types of interactions were considered: Mechanical interactions by adhesive and repulsive forces as well as mechanical friction forces, and intercellular communication via signaling molecules, including DAMPs (Damage-associated molecular pattern), PDGF (Platelet-derived growth factor), TGF $\beta$  (Transforming growth factor  $\beta$ ), CXCL1 (C-X-C motif chemokine ligand 1), and CCL2 (C-C motif chemokine ligand 2).

The interaction network of the different cell types was classified into highly probable “cl-1” (with direct experimental support) or probable “cl-2” (with indirect experimental support) (Fig. 1C).

There is a huge body of experimental data on specific aspects of the regeneration process that partially looks as alternative or backup mechanisms, which do not significantly modulate the liver regeneration model. We here focus on the plausible selection of those mechanisms emerging from the data that have been implemented in the model. We first detail these mechanism before discussing possible alternatives.

In the model, DAMPs are released by the injured hepatocytes (Brenner et al., 2013), e.g. to activate Kupffer cells (cl-1). This is based on the report that injured hepatocytes can release HMGB1 and HSP-79 (both are DAMP signals, Huebener et al., 2015, Calderwood et al., 2016, Li et al., 2020,) to activate Kupffer cells (Martin-Murphy et al., 2010) (cl-1). Platelets are recruited to the site of injury and bind with sinusoidal endothelial cells during the early stage of liver injury (Nowatari et al., 2014, Ramadori et al., 2019) (cl-1) to promote the proliferation of hepatocytes (Meyer et al., 2015) and synthesize PDGF (also synthesized by activated macrophages, Pinzani et al., 1994) (cl-1). PDGF acts on activated HSCs, which display upregulated PDGFR expression to induce proliferation and migration (Yang et al., 2003, Melton and Yee, 2007) (cl-1). In the model, the source of PDGF was simplified as the positions of sinusoids inside the dead region, of activated Kupffer cells and of infiltrating macrophages. TGF $\beta$  is synthesized by activated Kupffer cells based on the report that TGF $\beta$  is predominantly expressed in Kupffer cells (De Bleser et al., 1997) (cl-1). TGF $\beta$  acts on HSCs, which are highly responsive to that cytokine, and in most cases, TGF $\beta$  is described as prominent driver of activation (e.g., Cai et al., 2018, Fan et al., 2019) (cl-1); there are also cases described, where TGF $\beta$  is more involved in HSC survival than activation, whereby another factor secreted from infiltrating macrophages is a more prominent driver of activation (Imamura et al., 2005) (cl-2).



In the model, two different factors to activate HSCs were assumed: one is TGF $\beta$  that is provided by activation of ECM deposited Latent TGF $\beta$  (Fan et al., 2019), subsequently synthesized by the liver non parenchymal cells, that is, activated Kupffer cells, HSCs and LSECs. The other factor is an assumed alternate factor generated by activated infiltrating macrophages. Then, CXCL1 is synthesized by both activated Kupffer cells and HSCs to attract neutrophils (Kisseleva and Brenner, 2007, Marra and Tacke, 2014) (cl-1). CCL2 is synthesized by activated HSCs, Kupffer cells, infiltrating macrophages and sinusoids in the lesion region to attract infiltrating macrophage (cl-1). This is based on the report that activated stellate cells, Kupffer cells, macrophages, endothelial cells secrete CCL2 to control the macrophage infiltration (Baeck et al., 2012, Krenkel et al., 2014).

In the model, a subpopulation of Kupffer cells are assumed to be able to eliminate dead hepatocytes based on the observation that dead hepatocytes are engulfed by Kupffer cells (Canbay et al., 2003) (cl-1). Moreover, infiltrating macrophages are assumed to also eliminate dead hepatocytes as previously described (Boulter et al., 2012) (cl-2).

We have three additional hypotheses on the function of infiltrating macrophages. The first is to contribute to the activation of HSCs e.g. based on reports that infiltrating macrophages secrete at least one HSC activating factor (Imamura et al., 2005) (cl-2); the second is to induce death of the activated HSCs based on the report that infiltrating macrophages might trigger apoptosis of activated HSCs (Tacke and Zimmermann, 2014) (cl-2); the third is to revert the activated HSCs to the quiescent phenotype (Kisseleva et al., 2012, Troeger et al., 2012, Hassan, 2017) (cl-2). This is probably depending on different macrophage phenotypes/subpopulations, as becomes more and more evident from recent scRNASeq experiments (Willemsen and Winther, 2020).

One advantage of in silico modeling is to permit straightforward testing of all different selected regeneration scenarios, which may then serve as a guide to exclude those ones for experimental validation that by the simulations have to be assumed apriori to fail. This is demonstrated below by running simulations switching off or varying interactions labeled as “cl-2”, and therewith test the influence of each of the following interactions (and the combination of some of them) on the process of liver regeneration:

- (1) Infiltrating macrophages eliminate (or do not eliminate) dead hepatocytes (Fig. 1C, no. 22, cl-2);
- (2) DAMPs activate (or do not activate) infiltrating macrophages (Fig. 1C, no. 3, cl-2);
- (3) HSCs are activated by TGF $\beta$ , e.g. from Kupffer cells (no. 21, cl-2), or an alternate factor produced by infiltrating macrophages (no. 18, cl-2);
- (4) HSCs either attract or do not attract Kupffer cells to migrate (no. 24, cl-2);
- (5) Infiltrating macrophages revert activated HSCs to a quiescent phenotype (no. 19, cl-2), or induce cell death of activated HSCs (included in no. 19, cl-2).

If interactions (1) – (5) were all excluded, regeneration did not succeed in the model.

The model permits to study in how far alternative assumptions on cell-cell interactions, perturbations within each of them, or in selective ones impact on regeneration of the pericentral drug-induced lesion.

**State changes of cell types and timings:** The state changes of cell types concern attributes such as activation and deactivation, or initialization for differentiation, as we now know into multiple different functional phenotypes. The cellular consequences can be, among others, migration, reversion from activation, killing, proliferation and death, depending on the specific cell type (specified in table S2), and other parameters.

The timing of our simplified scenario was chosen in agreement with our own experiments (as in Fig. 1A) and from published references (Dragomir et al., 2012, Graubardt et al., 2017). For Kupffer cells, indications of a potentially constant cell population size were assumed. To challenge this assumption, we studied both, varying and constant Kupffer cell populations (see details in SI). In our model, the Kupffer cell population is considered as an input parameter and not a readout. Alternately, we could model Kupffer cell number kinetics as appearance and death process (death at days 1-2, appearance and spread from day 2 on), but this was not the purpose of this work.

**Model at cell & tissue level; cell geometry:** Hepatocytes, hepatic stellate cells, Kupffer cells and infiltrating macrophages, as well as neutrophils are modelled, each as individual entity. The endothelial cells are not modelled individually, but as part of a network of sinusoids. Each hepatocyte has been approximated by an isotropic, elastic, and adhesive sphere (Fig. 1D, white objects), named "center-based model" (CBM), capable of interacting with other cells or blood vessels by mechanical forces or chemical signals. The sphere can be thought as specifying the region in space where the hepatocyte is localized with overwhelming probability. The CBM has been parameterized by material and cell-kinetic parameters, which permits to readily identify the physiological parameter ranges. Macrophages and neutrophils were equivalently mimicked by a CBM, but with different cell parameters (Fig. 1D, green and brown objects). Different from the former cell types, the HSCs were approximated by an isotropic, elastic, and adhesive sphere with chains of elastic springs emanating from their body to capture their long protrusions (Fig. 1D, cyan objects). The sinusoidal network is modeled as semi-flexible chains of spheres that are connected by springs (Fig. 1D, red objects). This design accounts for the fact that vessels resist bending and stretching. The parameters of the sinusoids comprise volume, density and branching orientation, which are sampled from the scanning data of the real liver sinusoidal system (see more details in Hoehme et al., 2010).

**Model at cell & tissue level; force balance & cell movement:** Cell and sinusoid movement is computed based on force balance. The model takes into account passive and active forces. Passive forces are friction forces of each cell with its environment (other cells, sinusoids, intercellular medium), deformation and compression forces experienced by a cell, as well as cell-cell and cell-sinusoidal adhesion forces. Cell migration, as it occurs by anchoring of cells in

the extracellular matrix, e.g. in the space of Disse, is mimicked as an active force. The precise form of the forces (as detailed in the STAR METHODS) has been chosen to directly represent cell material parameters. For example, the cell-cell interaction force has been approximated by the "Johnson-Kendall-Roberts"(JKR)- force model for homogeneous elastic sticky spheres, which has been shown by micro-pipette experiments (Chu et al., 2005) to quantitatively reproduce the force-distance relation of two cells brought in contact and pulled apart. In conjunction with the friction force, the emerging behavior at the tissue level is viscoelastic. During liver regeneration, cell proliferation causes cell compression, which cannot be properly addressed by standard pair-wise forces (as JKR, Hertz etc.) (Van Liedekerke et al., 2015). To correct for this shortcoming, the JKR-force was modified for small cell-cell distances by a term that accounts for volume compression forces arising from large cell deformation, calibrating with the "Deformable Cell Model (DCM)" (Van Liedekerke et al., 2019).

The motion of cells and sinusoids is updated by solving an overdamped stochastic equation of motion, a Langevin equation, which summarizes all forces exerted on them:  $\sum F_{fri} + F_{def} + F_{adh} = 0$ , where  $F_{fri}$ ,  $F_{def}$ ,  $F_{adh}$  are friction force with the environment, deformation force, and adhesive force with other cells or elements, respectively (Fig. 1D, see more details of each force term in STAR METHODS).

**Model at cell & tissue level; molecular interactions:** Cell types may secrete signal molecules that are sensed by other cells. The spread of the molecules is mimicked by a diffusion equation. The cells generating the molecules are represented as source terms in the diffusion equation. Moreover, the equation contains a general first-order kinetics decay term (molecule degradation term in Fig. 1D, see more details of each equation term in STAR METHODS).

**Model parameterization:** Most model parameters and the liver lobule micro-architecture have been chosen as previously developed (Hoehme et al., 2010) (Table S1). The densities of non-parenchymal cells not considered in that reference has been estimated from other published references, as for neutrophils for example, from McDonald et al., 2010, Marques et al., 2014 (Table S1).

**Definition of a reference model:** The definition of a reference model is to some extent arbitrary. Here, it was guided by choosing all interactions from Fig. 1C that belong to cl-1 (consensus), plus all the interactions (1-5) of cl-2, as shown above, and which were verified to result in a functioning regeneration scenario in the simulation (as in Fig. 1E), in agreement with the experimentally observed lesion size and hepatocyte density (the details of interaction label and corresponding reference can be seen in Fig. 1C and Table S1).

### **Simulated regeneration scenarios with the reference and alternative interaction models**

**The reference model:** The simulation starts at day 0, right after injection of the hepatotoxic substance (CCl<sub>4</sub>/APAP). Hepatocyte injury is expected to occur in less than an hour, supported by fact that in mice, for example, the highest APAP blood concentration ("Cmax") is reached ~30 minutes after injecting the drug into the peritoneum (Sezgin et al., 2018, Schneider et al.,

2021, Schuran et al., 2021). The timing of the processes depicted in Fig. 1C follows the assumed logical order of the subprocesses finally resulting in a functioning regeneration (Fig. S2). In a first step, the direct effect of APAP on Cyp450 positive hepatocytes via NAPQI generation was included. This was realized by constructing a dose-dependent cell death induction in this subpopulation of hepatocytes, and the time (point) at which death occurs. Both parameters are based on experimental data in that the NAPQI-pathway displays a time and dose-dependent (in vitro: concentration dependent).

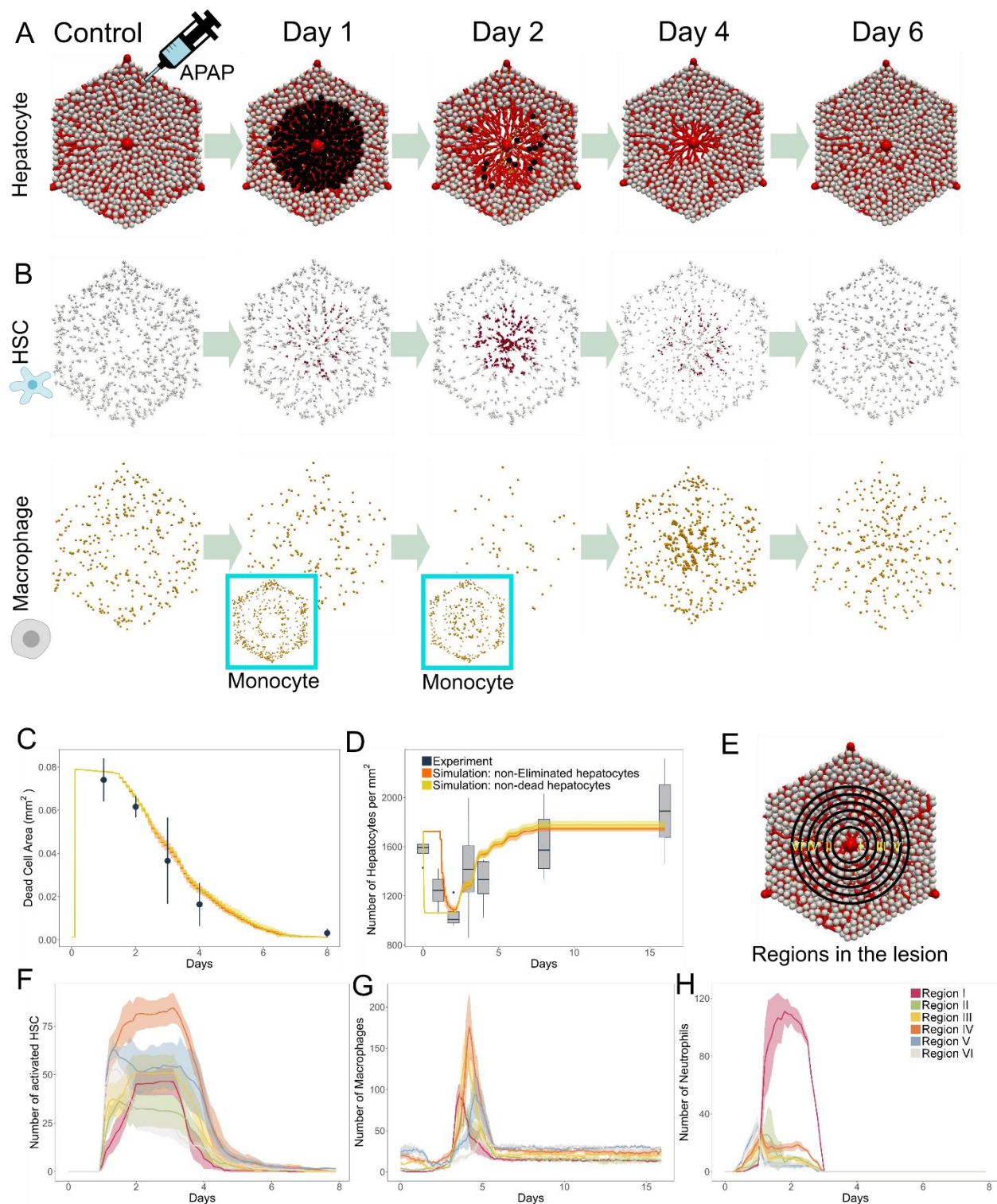


**Figure 2. Pattern of liver lobule regeneration (reference model).** (A) Simulated lobule, consisting of different cell types and the sinusoids over time, taking into account different simulation scenarios. White spheres are healthy hepatocytes, black spheres are dead hepatocytes; sinusoids are visualized as red lines. (B) The distribution of HSCs (dark red: activated; grey: quiescent) and macrophages (brown) over time. The distribution of Ly6C-high

monocytes on days 1 and 2 are shown in the blue boxes. Their precise spatial pattern depends on the timepoint of secretion and the range of CCL2. (C and D) Lesion area and number of hepatocytes over time from both, simulations and experiments. (E) Spatial distribution of activated HSCs, macrophages, and neutrophils in the lobule, measured by counting the corresponding cell number over the distance to the central vein (CV). As illustrated, there are six regions considered: Region I ( $< 21.4 \mu\text{m}$  to the CV), II (between  $21.4$  and  $42.8 \mu\text{m}$  to the CV), III (between  $42.8$  and  $64.2 \mu\text{m}$  to the CV), IV (between  $64.2$  and  $85.6 \mu\text{m}$  to the CV), V (between  $85.6$  and  $107 \mu\text{m}$  to the CV), VI (between  $107$  and  $128.4 \mu\text{m}$  to the CV). (F to H) Number of activated HSCs, macrophages, and neutrophils in all regions over time. Error bars represent the standard deviation of four simulation runs, using different random seeds.

In a second step, the timing of the interaction processes not directly depending on NAPQI (these were introduced above, are depicted in Fig. S2 and are based on information found in the references in Table S2 as well as on simulation-calibration) is explained, and related to the spatial-temporal pericentral hepatocyte damage and regeneration process depicted in Fig. 2A. In detail, before drug administration, both HSCs and Kupffer cells are distributed homogeneously in the lobule (Fig. 2B, quiescent/activated HSCs are colored in white/red and Kupffer cells are colored in brown). Up to about 1 hour after drug administration, injured hepatocytes secrete DAMPs that activate Kupffer cells, making them secreting CXCL1, TGF $\beta$  and CCL2. CXCL1 attracts neutrophils which migrate towards the Kupffer cells. At the same time, sinusoidal endothelial cells/platelets also localized in the region of the prospective lesion are secreting CCL2 and PDGF. PDGF attracts HSCs, which then cause migration of Kupffer cells towards them. Hence, two processes make Kupffer cells preferentially being activated in the prospective dead cell area: firstly, the secretion of DAMPs by hepatocytes in the prospective lesion, which force DAMP concentration to be higher for Kupffer cells in the prospective lesion than outside, and secondly, the fact that the Kupffer cells are attracted by the HSCs, which become activated, stimulated to proliferate and migrate towards the prospective lesion by the gradient of DAMPs, PDGF and chemokines. In-line with Fig. 1A, the population size of Kupffer cells has been modelled to drop after activation until day 2 and recover thereafter. Death has been mimicked by a death rate such that the decay could be qualitatively reproduced, the recovery has been modelled by adding new Kupffer cells with a certain rate. The diffusion length for DAMPs is about 3 cell diameters in 1 hour, so at the short time scale considered, the DAMPs do not spread over the entire lobule. Consequently, neutrophils attracted by CXCL1, migrate almost entirely towards the prospective lesion. Neutrophils in contact with injured hepatocytes are assumed to initiate their death reaching a state in which they become “flagged” for a potential elimination by macrophages after about 1 day. About the same time, TGF $\beta$  (probably in a first step derived from LTGF $\beta$  deposits in the ECM adjacent to the damaged hepatocyte area, activated by the dying hepatocytes) activates HSCs making them secrete CCL2 and CXCL1 amplifying and/or backing up the effect of Kupffer cells and platelets. Activated HSCs proliferate and secrete extracellular matrix (ECM) (Kisseleva and Brenner, 2021). Infiltrating macrophages are attracted by CCL2 approaching the dead hepatocytes. The infiltrating macrophages are initiated as monocytes with Ly6C-high phenotype, which do not show up in the macrophage population in Fig. 2B. However, those monocytes (inset to Fig. 2B) that are in the range of CCL2 move during the two days towards the hepatocyte damage region. After a

period of time between 2 and 3 days, the infiltrated monocytes transform into macrophages with Ly6C-low phenotype (Zigmond et al., 2014, Graubardt et al., 2017). They can phagocytose the dead hepatocytes when they are at Ly6C-high phenotype. Once they adopted the Ly6C-low phenotype, they can phagocytose or revert activated HSCs (Tacke and Zimmermann, 2014). The Kupffer cell population drops in the first two days due to toxic damage (Ritz et al., 2018) (Fig. 2B), and recover from day 2 on. The recovered Kupffer cells can, as the Ly6C-low phenotype, phagocytose the dead hepatocytes, as well as the ECM that has been deposited by activated HSCs (after repeated administration of CCl<sub>4</sub> or APAP, ECM deposition becomes significant, Ghallab et al., 2019).

This leads to a clearance of the lesion from dead hepatocytes, while it may still be populated with activated HSCs and macrophages (Fig. 2B, day 2). Around day 1.5-2, hepatocytes outside of the dead lesion start to enter S-phase to eventually replace the dead hepatocytes (Hoehme et al., 2010). Sinusoids located in the lesion are among the prime candidates for HGF and EGF secretion, which are both mitogens for hepatocytes (Michalopoulos 2010, 2017). After about 3 days, macrophages begin to deactivate HSCs. At day 6, the lesion is closed by healthy hepatocytes having replaced the removed (dead) hepatocytes (Fig. 2B). In different simulation runs, we find sporadic dead hepatocytes that are later phagocytosed, while in some simulations the dead hepatocytes have been entirely eliminated by day 6 and the lesion was closed. Infiltrating macrophages have already disappeared. The HSCs become deactivated, and both, HSCs and Kupffer cells redistribute in the lobule (Fig. 2B), the latter accompanied and driven by a change of fate from Ly6C-high phenotype to Ly6C-low phenotype (see details in STAR METHODS).

In a next step, the spatial temporal distributions were quantified. For the lesion area and hepatocyte density over time, for which we had quantitative experimental values (Hoehme et al., 2010), the simulation results show a perfect agreement to the experimentally observed values (Figs. 2C, D). In Hoehme et al., 2010, the lesion area was experimentally defined as the area not containing hepatocyte nuclei anymore, while signs of cell death occurred already earlier, but were not considered in the experimental curve (SI to that reference). Referring to the direct effect of NAPQI, the lesion may alternatively be assessed regarding the lobule space not occupied by "healthy" hepatocytes, in which case the dead cell area shows up earlier as in Fig. 2C, different from the previous model that did not take into account the direct effect by NAPQI-detoxification (Hoehme et al., 2010). Following the same line of argument, the hepatocyte density maybe defined as the number of hepatocytes over the area of the lobule (as in Hoehme et al., 2010) or the number of healthy hepatocytes over the area of the lobule. Both measures result in different spatial profiles before 2 days after the injury. In Fig. 2D we depicted the number of healthy hepatocytes, which may be difficult to demarcate from those already damaged and about to die in the experiment.

We lacked quantitative values for the other cell types, so estimated their density from published references (Bouwens et al., 1986, Wake, 2006, McDonald et al., 2010, Zigmond et al., 2014) and measured in the simulation the change of their profile, which may be seen as a mainly qualitative model prediction. In order to simulate the dynamic change of the distributions of HSCs, macrophages (both Kupffer cells and infiltrating macrophages), and

neutrophils, the lesion region was divided evenly into 6 sub-regions according to their distance to the CV (Fig. 2E), and the number of each type of sinusoidal cell type in each sub-region was counted over time. As shown in Fig. 2F (experimental: Fig. S1D), the number of activated HSCs starts to rise after day 1, probably driven by TGF $\beta$ , provided by activation of its latent form from the ECM, and subsequently from de novo production by Kupffer cells. This parallels with Kupffer cells beginning to eliminate the bodies of dead hepatocytes (Canbay et al., 2003). The number of activated HSCs is highest in region I, which is located most close to the CV. The number of activated HSCs peaks around day 2, then dropping dramatically due to the interventional effect of Ly6C-low expressing infiltrating macrophages, which induce cell death and/or reversion to quiescence (Ritz et al., 2018, Fischer et al., 2002). NK (natural killer) and NKT (natural killer T) cells also contribute to induce death of activated HSCs (Gao and Radaeva, 2013). At around day 6, there are no activated HSCs left in the lobule. As shown in Fig. 2G, the number of macrophages in the pericentral area decreases before day 2, probably from toxic damage upon phagocytosing the dead hepatocytes. After day 3, the Kupffer cell number quickly rises again, due to repopulation of the pericentral area by proliferation and migration of the resident Kupffer cells and/or differentiation from the massively infiltrating macrophages into the lesion. After day 4, the macrophage population in the lesion drops again, this time due to depletion of infiltrating macrophages (Zigmond et al., 2014). After around day 6, the number almost resumes to initial values, e.g. resulting from the Kupffer cells relocating back to their initial distribution. As shown in Fig. 2H, the number of neutrophils rises quickly after day 0, attracted by a CXCL1 gradient and in order to deplete the injured hepatocytes. Recruited neutrophils accumulate in region I and the number rises until day 1. Until day 3, the neutrophil population disappears.

Our simulation of the reference case can achieve the expected pattern of normal liver regeneration and agree with the experimentally observed dynamics for the necrotic lesion size and hepatocyte density.

Next, we explored the communication between different cell types and factors to achieve liver regeneration after NAPQI induced damage by testing type “2” interactions (probably happening *in vivo*) in the network.

#### **Alternative cell-cell interaction network models:**

In a next step variations of the reference model (RM) were considered by individually modifying the following five interactions of the reference network: (1) Infiltrating macrophages cannot (RM: can; no. 22) eliminate the dead hepatocytes; (2) Infiltrating macrophages are not activated by DAMPs (RM: are activated; no. 3); (3) HSCs are activated by another factor, besides TGF $\beta$ , which is produced by activated macrophages derived from infiltrating monocytes (RM: TGF $\beta$  is activating HSC, no. 21; we assumed that this factor has about the same diffusion constant as TGF $\beta$ ); (4) HSCs cannot attract Kupffer cells to migrate (RM: they do, no. 24); (5a) Infiltrating macrophages deplete activated HSCs (Fig. S6A-S6E); (5b) 50% of activated HSCs are depleted/50% are reverted (Fig. S6G) (RM: infiltrating macrophages revert activated HSCs to quiescent phenotype, no. 19).



Below, we refer to a model, in which the assumption ( $k$ ;  $k=1, 2, 3, 4, 5$ ) has been modified as model. As shown in Fig. 3A, C, D, the alternative models (2) and (5) do not significantly alter the result of the reference model regarding a complete liver regeneration, while the modifications (1), (3), and (4) influence the lesion recovery in that regeneration after 16 days is still incomplete. Fig. 3A displays a single simulation scenario, where dead hepatocytes are colored in black. Fig. 3C shows the average over 4 runs with different random seeds. Among the perturbations (1), (3) and (4), the area of the unhealed lesion is largest for model (1), probably due to the inhibition of phagocytosis of infiltrating macrophages. The Kupffer cells alone are not able to clear dead hepatocytes in time. However, a parameter sensitivity analysis suggests that Kupffer cells equipped with a stronger phagocytosis capacity, by a shorter elimination duration, would alone be able to clear the necrotic area from dead hepatocytes in the experimentally observed time (Fig. S6H; matching with the RM). The importance of infiltrating macrophages in clearing up the lesion is also indicated by the modification implemented as model (3), where HSC activation is depleted (Fig. 3B and Fig. S4D). Due to the lack of activated HSCs in the lesion, the expression level of CCL2 is not sufficient to attract infiltrating macrophages into the lesion to clear up dead hepatocytes (Fig. 3B, Fig. S4C, and Fig. S5B). Similar to model (3), in model (4) the number of Kupffer cells in the lesion is much smaller than that in the reference case, hence less TGF $\beta$  is produced in the lesion resulting in decreased numbers of activated HSCs (Fig. 3B, Fig. S4D, and Fig. S4C). Again, the expression level of CCL2 is reduced, and as a consequence, fewer infiltrating macrophages are attracted into the lesion, as compared to the reference case (Fig. 3A and Fig. S4C).

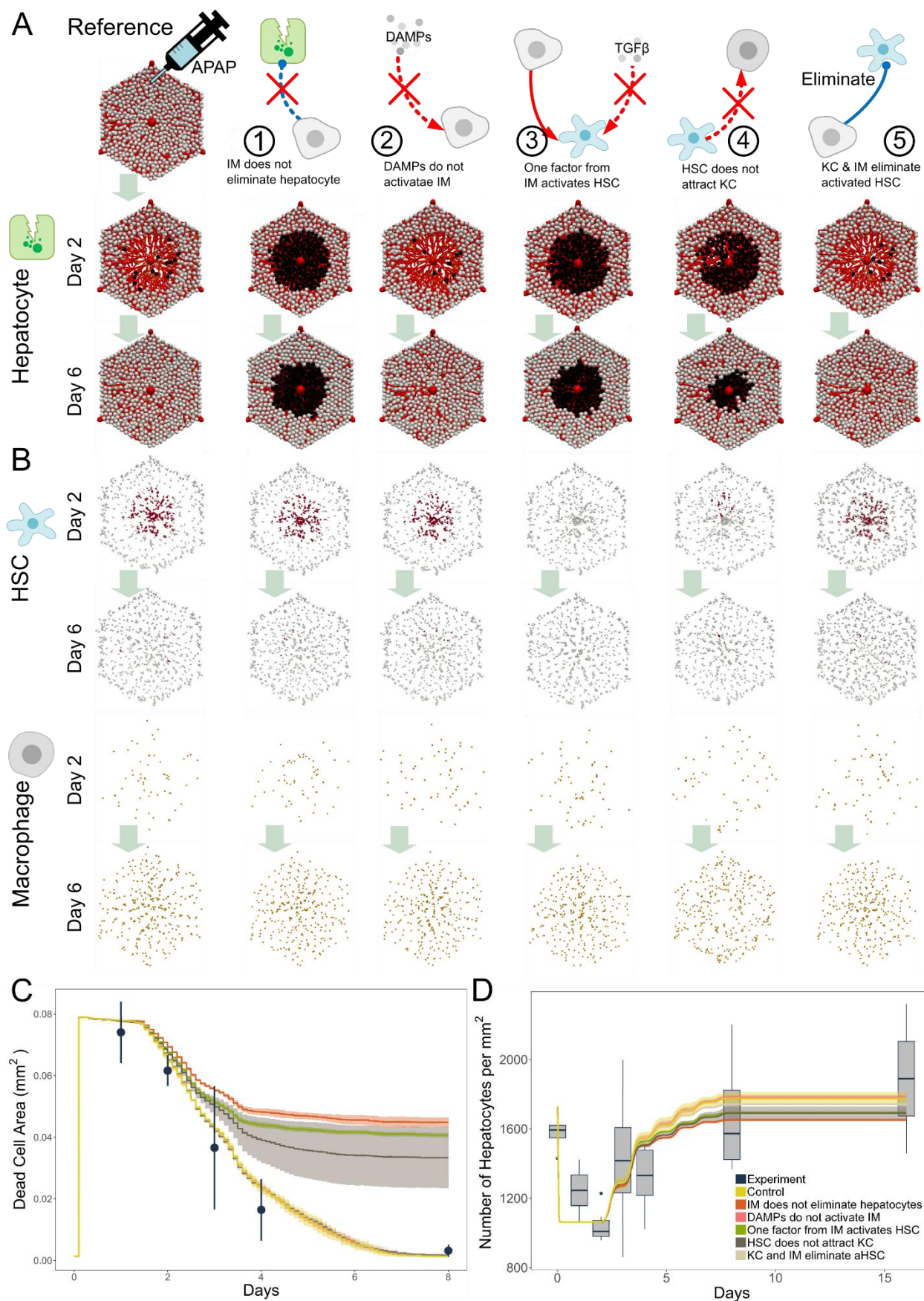


**Figure 3. Pattern of liver lobule regeneration resulting from alternative interactions.** (A) The regenerating lobule over time under reference and five alternative interactions: (1) Infiltrating macrophages do not eliminate dead hepatocytes; (2) DAMPs do not activate infiltrating macrophages; (3) HSCs are not activated by TGF $\beta$  but by one factor from infiltrating macrophages; (4) Kupffer cells do not migrate towards HSCs; (5) Kupffer cells and infiltrating macrophages eliminate activated HSCs instead of reverting them to quiescent mode. (B) The distribution of activated HSCs (antibody:  $\alpha$ SMA) and macrophages (antibody: F4/80) over time under reference and five perturbed interactions. (C and D) Lesion area and hepatocyte density over time under reference and five alternative interactions.

We further tested a model simultaneously implementing assumptions (2) and (5), which did not have significant impact on liver regeneration (Fig. S6F-S6H).

Our computational study of these five individually modified interactions suggests two main conclusions: (1) There is a positive feedback loop between Kupffer cells and HSCs, where the presence of HSCs promotes migration of Kupffer cells into the lesion, while increasing numbers of Kupffer cells in the lesion increase the number of activated HSCs, which attract more infiltrating macrophages to help clear up dead hepatocytes; (2) The way to diminish activated HSCs by macrophages, either by engulfment or by phenotype reversion has no significant impact on lesion recovery. Note however, that in case HSCs are depleted, the remaining HSCs would have to proliferate to repopulate the lobule to its original population size. It is now obvious from experimental data that half of the population of activated HSCs is depleted and half of it is reverted, which by itself would more or less lead to repopulation of the liver to the original healthy state (Kisseleva and Brenner, 2021).

In a next step, we test how far simulations of perturbation scenarios are suited to guide experiments in a way to permit pinpointing differences between interaction mechanisms at the tissue level, and hence serve to validate the model predictions.

### **Simulated perturbation experiments: Depletion of non-parenchyma cells**

After the simulated testing of the reference model and of variations that differ from the reference model by one interaction, additional perturbation simulations were performed to predict the impact of depletion of cells typically found along the sinusoidal network spaces on liver regeneration. In each of four perturbation simulations (I-IV), one of the four cell types HSCs, Kupffer cells, infiltrating macrophages and neutrophils was depleted individually.

A further advantage of the model is that it permits to test hypothetical cases and see how much contribution to an observed effect can be attributed to sub-processes. Both will be discussed below.

### **Perturbation I: The model predicts that depletion of HSCs results in an unhealed lesion**

The depletion of HSCs (Fig. 4A, scenario 1) did not change the size of the lesion induced by the drug and characterized by dead or dying hepatocytes. This turns out to be the same for all cell type depletions, indicating that the lesion size is mainly controlled by the cell death caused

downstream of the NAPQI pathway. In the case of HSC depletion, however, the dead hepatocytes are not cleared up. Due to the lack of activated HSCs, CCL2 levels are not sufficient to attract infiltrating macrophages to clean up dead hepatocytes. In addition, due to the absence of HSCs, Kupffer cells do not migrate. Consequently, the number of Kupffer cells in the lesion is smaller than in the reference case. This is similar to the perturbation that disables HSCs to attract Kupffer cells to migrate (scenario 4, Fig. 3A). In general, depletion of HSCs leads to reduced numbers of neutrophils, Kupffer cells, and infiltrating macrophages in the lesion. As a consequence, a large number of dead hepatocytes remains uncleared in the lobule.

Our prediction is consistent with a previous study, where the depletion of HSCs resulted in decreased expression levels of CXCL1 and reduced numbers of infiltrating neutrophils (Stewart et al., 2014).

**Perturbation II / III: The model predicts that depletion of macrophages abrogates clearance of lesion from dead hepatocytes, independent on whether it concerns the Kupffer cells or the infiltrating macrophages.**

As shown in Fig. 4A (scenario 2), after depletion of Kupffer cells, the necrotic lesion is only marginally cleared up from dead hepatocytes. Due to the lack of Kupffer cells, there is a reduced TGF $\beta$  signal to fully activate HSCs, leading to qualitatively the same scenario as above after depletion of HSCs. As Kupffer cells are totally missing, phagocytosis by Kupffer cells does not take place, leaving even more dead hepatocytes in the lesion than in the previous case. We further tested if HSCs can be activated even after depletion of Kupffer cells, we found that the lesion can be recovered in time (Fig. S6G). These results indicated the importance of activation of HSCs in regulating lesion recovery.

After the depletion of infiltrating macrophages (scenario 3 in Fig. 4A), again a large part of the dead hepatocytes remains in the lobule not being cleared. This is similar to the perturbation of disabling infiltrating macrophages to eliminate dead hepatocytes (Fig. 3A, scenario 1).



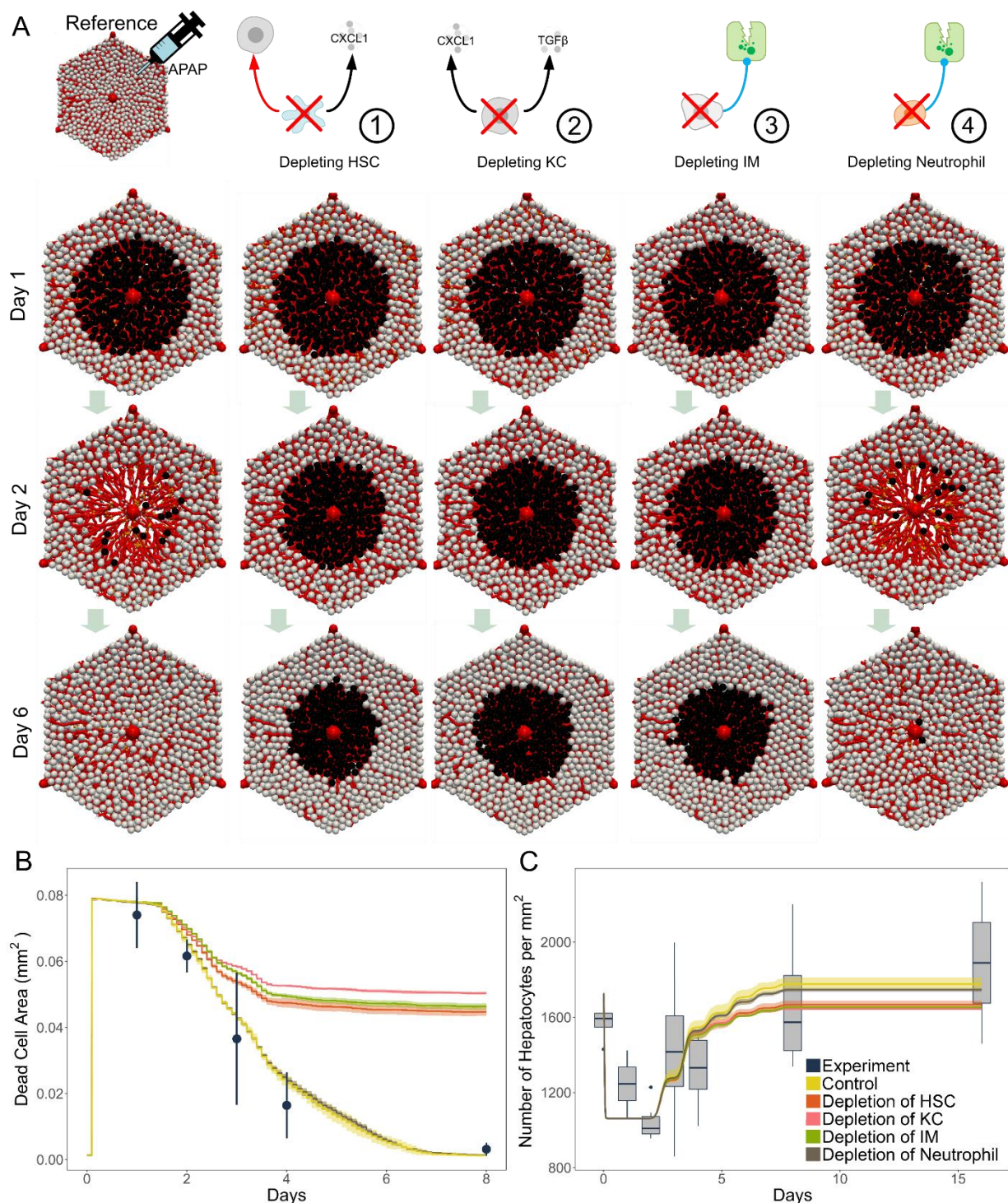


**Figure 4. Pattern of liver lobule regeneration upon depletion of different cell types in the reference model (Fig. 2).** (A) The regenerating lobule over time as reference state and upon depletion of four sinusoidal cell types: (1) Depletion of HSCs; (2) Depletion of Kupffer cells; (3) Depletion of infiltrating macrophages; (4) Depletion of neutrophils. (B and C) Lesion area and hepatocyte density over time in the reference state and upon depletion of different cell types as indicated.

Our prediction is consistent with a previous study of depleting infiltrating macrophages in acute liver injury, which resulted in delayed tissue recovery (You et al., 2013).

Because of the (expected) dramatic effect of macrophage depletion on the regeneration result, we refined the assumed perturbation by replacing the dynamic kinetics of Kupffer cell numbers in the course of the regeneration process by assuming a constant population size after the 6-hours time point.

For this case (Fig. S8), we found no consequence on the readout parameters at day 6, interestingly indicating that the precise dynamics of the Kupffer cell population may not be a critical determinant of the regeneration process, as long as Kupffer cells are present for being activated by damaged hepatocytes through DAMPs, and to facilitate HSC activation early (about one hour) after drug administration.

#### **Perturbation IV: The model predicts that the depletion of neutrophils has no significant influence on liver regeneration**

As shown in Fig. 4A, after simulation the depletion of neutrophils, there is neither a significant effect on the generation of damage, nor on the regeneration of the necrotic lesion in comparison to the reference scenario. Therefore, neutrophils might be considered as providing backup mechanisms to induce damage towards epithelial cells, to phagocytose the damaged debris, and to induce cell death in HSC (Kisseleva and Brenner, 2021). This is in-line with ref. (Krenkel and Tacke, 2014), stating that cell death induced by neutrophils in APAP-induced liver injury is not very obvious *in vivo*, even though it can be observed *in vitro* (Marques et al., 2012).

This still needs further debate, as an older study of depleting neutrophils during acute liver injury reported protection of the lobule against hepatotoxicity with a significantly reduced centrilobular necrosis area (Liu et al., 2006). As the latter was not the case in our simulations for the hypotheses studied in the main body of this work, it prompted us to investigate a further highly speculative case, that may not be expected in acute liver damage, but perhaps could be obtained by proper experimental manipulations (Fig. S7). Here, we consider regeneration from a necrotic lesion that has not been generated by cell-death due to the NAPQI-pathway. The NAPQI pathway is for example not activated in hepatocytes that lack Cytochrom-P-450 enzymes, as occurring during periportalization after repetitive administration of APAP (or CCl<sub>4</sub>; Ghallab et al., 2019), and another hepatotoxic insult would be responsible for the multicellular necrotic lesion. In that simulation, for simplicity, we assumed also a circular necrotic lesion that initiates phagocytosis of dead hepatocyte debris by neutrophils and macrophages. Here, we could observe a protective effect against hepatotoxicity upon neutrophil depletion (Fig. S7). The simulations demonstrate that our framework may permit *in silico* tests of hypotheses that may not be present as such in nature, but may be realized by proper engineered manipulations.

## DISCUSSION

In our study, we developed a multi-level computational model of a virtual liver lobule that integrates an intercellular network of major hepatic cells and takes into account cell-cell communication based on selected published knowledge. We applied the model to simulate the liver regeneration process after APAP-induced acute hepatotoxicity and tested documented and hypothesized interactions between cells and signals. Furthermore, we made testable predictions on perturbations that were already performed in previous experimental studies.

Our virtual liver twin illustrates that testing or perturbing the intercellular communication between cells and signals allows exploring the mechanism behind liver regeneration and guiding the design of relevant experiments. The *in silico* liver considered here includes reported and hypothesized interactions between cell types, mediated both mechanically and by chemical signals. It permits to study alternative hypotheses and their consequences on the regeneration process. A plausible candidate model implemented the following temporal events: (1) Injured hepatocytes produce DAMPs and are killed via cell stress from APAP detoxification by NAPQI (Fig. S2). Platelets in the lesion produce PDGF; (2) Moreover, Kupffer cells and HSCs are also activated by DAMPs. The so activated HSCs are assumed in agreement with our data to be not detected through  $\alpha$ SMA, and migrate towards the gradient of PDGF; (3) activated non-parenchymal cells (and damaged hepatocytes) produce CXCL1, while neutrophils migrate towards the gradient of CXCL1 and induce death in injured hepatocytes; (4) Kupffer cells migrate towards the cluster of HSCs; (5) Activated Kupffer cells produce TGF $\beta$  to activate another function of HSCs, namely the production of CCL2 to attract infiltrating macrophages into the lesion. We assume that those HSCs are labelled by  $\alpha$ SMA; (6) infiltrating macrophages along with Kupffer cells engulf and eliminate the bodies of dead hepatocytes; (7) the healthy hepatocytes surrounding the lesion proliferate and collectively migrate towards the lesion to recover the lost hepatocytes, following a tug-of-war mechanism (Trepats et al., 2009; Hoehne et al., 2010; 2022); (8) Infiltrating macrophages switch from Ly6C-high phenotype to Ly6C-low phenotype to revert the activated HSCs into quiescent HSCs, whereas activated Kupffer cells switch back to quiescent Kupffer cells; (9) To restore the original cell distribution, we simulated alternative scenarios. Either HSCs previously localized in the lesion may die and be phagocytosed by macrophages, and those outside the lesion could proliferate. Another, perhaps more hypothetical scenario was the migration of quiescent Kupffer cells and HSCs. In a computer simulation comparing both scenarios (not shown) the regeneration of the necrotic hepatocyte lesion turned out to be insensitive to the precise mechanism of restorage of the original cell distribution. During the entire process, different types of hepatic cells interact and collaborate to achieve a perfect liver regeneration in time.

An important advantage of this virtual liver is that it permits to investigate the role of individual cell types and different signals by simulations. For example, the presence of one or several factors as well as its interaction with other factors can be depleted completely, weakened or amplified, and the consequence of this modification on the regeneration process and its final outcome can be studied. This may be impossible in an *in vivo* experimental model due to several reasons. Firstly, some modifications are technically not feasible or accompanied with huge effort. Secondly, possible backup mechanisms may hide the effect of a given change such

that the direct and indirect consequences are not detangled. Moreover, model simulations may show that certain manipulations are likely not resulting in a significant change of outcome, and therefore are not sufficiently informative to justify the effort of experimental realization, especially in regard to the 3R for animal experimentation. On the other hand, differences in the outcome of experiments and model simulations may indicate so far un-recognized mechanisms that would remain hidden without such simulations of a reference situation.

To demonstrate opportunity and power provided by the virtual liver, we simulated a number of perturbation experiments and presented their result as one of three possible basic scenarios, as follows (Fig. 5).

**Incomplete regeneration (Fig. 5, blue scenario):** An incomplete regeneration with dead hepatocytes remaining in the drug-induced lesion is predicted if either the infiltrating macrophages are lacking phagocytotic activity (scenario 1 in Fig. 3A), or are completely depleted from the lobule (scenario 3 in Fig. 4A). This suggests that the Kupffer cells, which are the resident macrophages, are insufficient to clear the lesion. This is still the case, even if their dead body elimination time is reduced from 3 hours (Haecker et al., 2002) to 6 minutes (Fig. S6H). The Kupffer cells are observed to engulf the dead hepatocytes (Canbay et al., 2003) while the infiltrating macrophages are hypothesized to remove the dead hepatocytes *in vivo* in ref. (Boulter et al., 2012). Our simulation (scenario 1 in Fig. 3) strongly support this hypothesis as depleting the phagocytosis ability of infiltrating macrophage leads to incomplete regeneration. However, one may argue that if the Kupffer cells have a sufficiently strong ability to phagocytize dead cells, they might in principle clear the lesion alone. Our model permits to specify the parameters under which this would be the case.

Seki et. al. (2007) observed *in vitro* that stimulated HSCs attract Kupffer cells to migrate towards them. Within our model we could show the prospective effect of such a mechanism *in vivo*: by depleting Kupffer cells or inhibiting Kupffer cells to migrate towards the concentrated HSCs in the lesion, there are also uncleared dead hepatocytes remaining in the lesion (scenario 4 in Fig. 3A and scenario 2 in Fig. 4A), suggesting that the relation observed by Seki et. al. (2007) *in vitro* should indeed be present *in vivo*, not requiring an *in vivo* study in the first place, where the conditions are more complex and difficult to control. I.e., the simulation indicates that in such a case as for the *in vitro*-finding by Seki et. al. (2007) an *in vivo* validation experiment (as it had been done) is promising to perform hence the resources (e.g. time, money, material, personnel) are likely well invested. In that sense, simulations with our model can guide the experimental strategy. When we depleted the HSCs from the lobule or disabled the activation of HSCs, for example through TGF $\beta$  produced by Kupffer cells, a similar unhealed lobule resulted (scenario 3 in Fig. 3A and scenario 1 in Fig. 4A). Together, the simulations suggest that the key to clear up the lesion is to attract a large enough number of macrophages in time to eliminate the dead hepatocytes. This requires the help of HSCs, e.g., to guide the migration of both Kupffer cells and infiltrating macrophages into the lesion.

**Reduced or no lesion (Fig. 5, yellow scenario):** The role of neutrophils is complex and controversial, some studies have shown that a lack of neutrophils does not affect the outcome or severity of APAP-induced liver injury (Krenkel and Tacke, 2014), while other studies indicated



that the neutrophils can directly mediate hepatocyte death in APAP-induced liver injury (Marques et al., 2012). We suggested that this might be due to the effect of NAPQI-induced cell death in the recent study (Ghallab et al., 2019). The majority of hepatocytes in the lesion are killed through NAPQI-induced detoxification. Therefore, the cell death induced by neutrophils in APAP-induced liver injury is not very obvious *in vivo* (Krenkel and Tacke, 2014), but can be observed *in vitro* (Marques et al., 2012). To test this assumption, we abrogated NAPQI-induced cell death, in which we found the majority of the hepatocytes in the lesion are killed by neutrophils. This is in agreement with the indication that neutrophils can mediate hepatocyte death. Furthermore, we abrogated NAPQI-induced cell death and depleted neutrophils. The lobule was surprisingly protected with no dead hepatocytes present (scenario 4 in Fig. S7A). This is another example of how our model can be used to test if or/and within which parameter ranges certain hypothesized mechanism have an observed effect.

**No effect on lesion generation nor on regeneration (Fig. 5, black scenario):** However, if NAPQI-induced cell death is not affected, the depletion of neutrophils has no significant impact on liver regeneration (scenario 4 in Fig. 4A). This result indicates that the neutrophil-induced cell death is supplementary to the NAPQI-induced cell death. Even if the latter is disabled in the simulation, the neutrophils can still kill the Cyp450 hepatocytes to generate room for the dependent new proliferation generated hepatocytes. In addition, the repopulation of the regenerated liver with quiescent HSCs, subsequent to (1) reversion of activated HSCs back to the quiescent phenotype by macrophages, and (2) inducing cell death of activated HSCs by macrophages or neutrophils, has no significant effect on the lesion regeneration (scenario 5 in Fig. 3A). Furthermore, we also tested the case if HSCs are activated in the early stage (right after the injury). As shown in Fig. S6G, when HSCs are activated first and migrate afterwards or in the case when KCs are depleted, HSCs can still be activated, both have no significant effect on lesion regeneration.

In conclusion, we have demonstrated the possible benefit and opportunities of a virtual liver to simulate, in this case, liver regeneration after acute damage in control and perturbation cases, at the level of a lobule and its constituting cell types, in time and space.

This may also include situations that can only be attained upon complex engineered manipulations, e.g. to explore potential therapy or protection effects. The model can be further developed and specified to simulate physiological and pathophysiological scenarios of liver and liver diseases. For example, in order to capture complex hepatocyte shapes as it occurs during fatty liver disease, fibrosis, cirrhosis or hepatocellular cancer, the cuboidal hepatocyte model

may be replaced by a cell model at higher spatial resolution (Van Liedekerke et al., 2019, 2020).

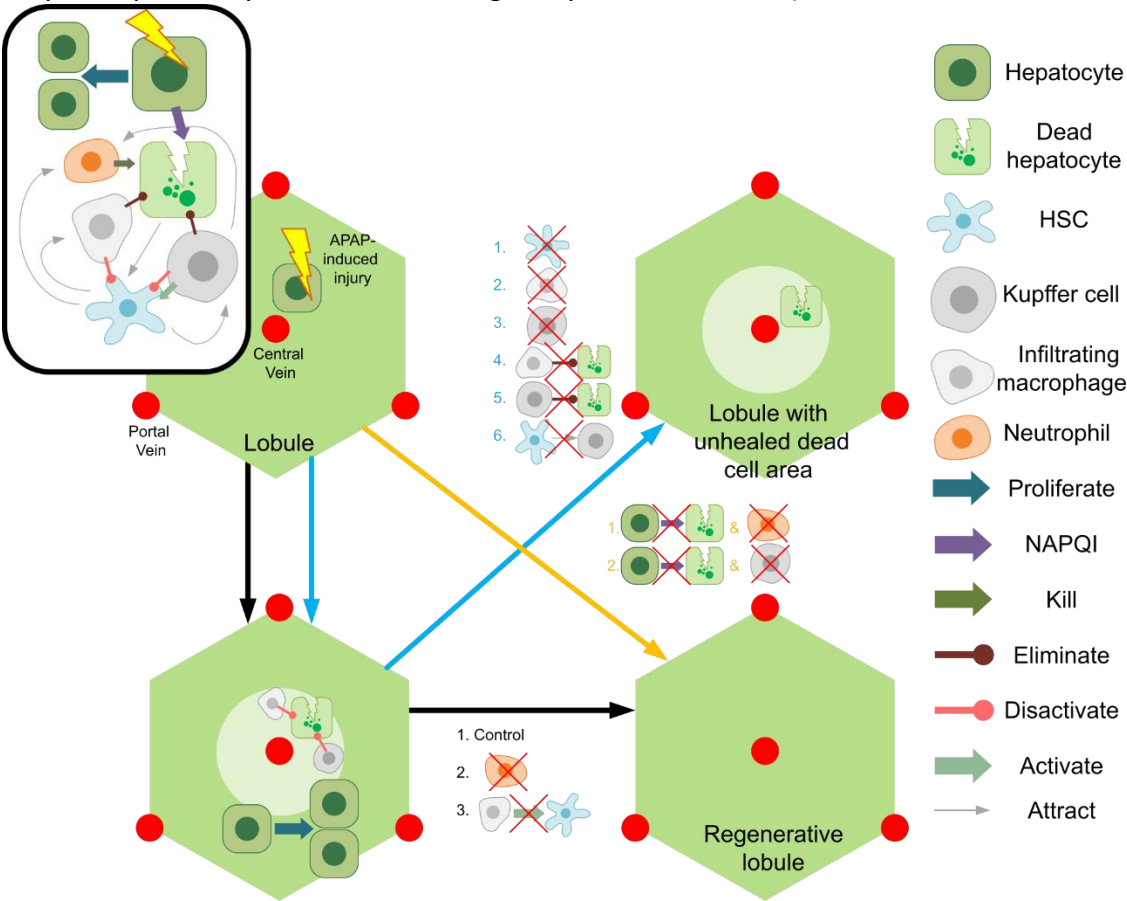


**Figure 5. Summary of the construction and application of the virtual liver twin to study liver regeneration after acute damage.**

Limitations of the study: A precise determination of the threshold concentrations in the simulation was not possible as the data were not present, and as the precise orchestration of molecular factors was and could not be mimicked in great detail. The underlying parametrisation concept was to choose plausible values out of accessible parameter ranges and infer parameters by comparison of their effect on the regeneration process. The robustness of the so determined parameters was studied in simulated sensitivity analyses. Nevertheless, it cannot be fully excluded that some parameters could in reality be outside of the ranges. However, this is not critical: the parameters / mechanisms that have been found to critically modify the regeneration process compared to the experimental observation should be challenged by additional experiments, whose outcome would then serve to re-calibrate the model parameter if necessary. Such an iterative procedure – identification of critical parameters and / or mechanisms by the model simulation – then experimental testing – then re-calibration of the digital liver twin model, will ultimately lead to a full quantitative digital twin model of liver generation.

In summary, we show the potential of our *in-silico* liver to successfully simulate liver physiology, and therewith present a promising strategy towards a full digital liver twin, that permits to test

perturbations from the molecular up to cell, tissue and body scales. We are not expecting it to replace experiments, but guiding towards the most informative experiments by identifying gaps in mechanistic knowledge. Such a liver twin is a key milestone on the route to guide diagnosis and therapy if fed with patient data. In so far, our work responds on the question of systems complexity.

## **MATERIALS & METHODS**

### **EXPERIMENTAL METHOD**

#### **Induction of acute liver injury by acetaminophen**

Acetaminophen (APAP)-induced acute liver injury was done in 10-week-old, male C57BL6/n mice (Janvier Labs, France), as previously described (Holland et al., 2022). Briefly, a dose of 300 mg/kg APAP was administered intraperitoneally into overnight fasted mice. Liver tissue samples were collected time-dependently, as indicated in the results section, and were processed for immunohistochemistry, as previously described (Campos et al., 2020, Gianmoena et al., 2021). All experiments were approved by the local animal welfare committee (LANUV, North Rhine-Westphalia, Germany, application number: 84-02.04.2016.A279).

#### **Immunohistochemistry**

Immunostaining of macrophages and activated hepatic stellate cells was performed in 4  $\mu$ m-thick paraffine-embedded liver tissue sections using an autostainer (Discovery Ultra Automated Slide Preparation System, Roche, Germany), as previously described (Schneider et al., 2021). The used antibodies and the staining conditions are summarized in the key resources table.

### **COMPUTATIONAL MODEL AND METHOD DETAILS**

#### **Agent-based modeling of cells and elements**

To capture their approximate shape, hepatocytes, macrophages, and neutrophils are approximated as spheres within a "center-based model"(CBM)-approach, which mimics the forces between cells as forces between their centers (Van Liedekerke et. al. 2015). Within the CBM-concept, the spherical shape does not represent the precise cell shape but region in space where the cell is located at with overwhelming probability. An HSC is modeled as a sphere forming the cell's core body, connected to four semi-flexible chains of spheres; sinusoids are modeled as semi-flexible chains of spheres. Such spheres can for example readily be constructed from inscribing spheres of maximal radius into image volume data sets stained for endothelial cells (e.g., by CD31) (e.g. Rohrschneider et al., 2007). During each time step  $\Delta t$ , the velocity  $\vec{v}_i$  of each sphere  $i$  is calculated according to one Langevin equation (an overdamped stochastic equation) of motion . The new position of  $i$  is then updated to  $\vec{p}_i(t) + \vec{v}_i(t)\Delta t$ , where  $\vec{p}_i(t)$  is the position of  $i$  at time  $t$ . Since HSCs, macrophages and neutrophils are either all located inside, wrap around, or migrate along sinusoids, we assume that they always remain in contact with a sinusoid edge (for HSC, the core body is sticking on the sinusoid edge). Therefore, the vector  $\vec{v}_i\Delta t$  for one HSC, macrophage, or neutrophil  $i$  is projected onto the line

of sinusoid edge to which  $i$  is in contact with. The position of  $i$  is then updated as  $\vec{p}_i + \vec{e}_i(\vec{v}_i \Delta t \cdot \vec{e}_i)$ , where  $\vec{e}_i$  is the unit orientation vector of the local tangent to the sinusoid to which  $i$  is connected with. The equations of motion for each type of cell and element are defined below.

**Equation of motion for hepatocytes.** Each hepatocyte is represented as a homogeneous isotropic, elastic, adhesive sphere. It can migrate, grow, divide, and interact with other cells or sinusoids. The position of hepatocyte  $i$  is updated from:

$$\Gamma_{ECM,i} \vec{v}_i + \sum_j \Gamma_{i,j} (\vec{v}_i - \vec{v}_j) = \sum_j \vec{F}_{ij} + \vec{F}_{mig,i}, \quad (1)$$

where  $\Gamma_{ECM,i}$  is the friction coefficient with the extracellular matrix (ECM, which is not explicitly modeled in this study),  $\Gamma_{i,j} = \gamma_{\perp}(\vec{e}_{ij} \otimes \vec{e}_{ij}) + \gamma_{\parallel}(I - \vec{e}_{ij} \otimes \vec{e}_{ij})$  is the friction tensor between cell  $i$  and the sphere  $j$  of other cell type (e.g. hepatocyte  $j$ ) or sinusoid sphere, and  $\vec{e}_{ij}$  is the unit vector from  $i$  towards  $j$ ,  $\vec{F}_{ij}$  is the corresponding central repulsion/adhesion interaction force,  $\vec{F}_{mig,i}$  is an (active) migration force of cell  $i$ . The central force is computed by (Popov, 2010):

$$\vec{F}_{ij} = \left( \frac{4\hat{E}}{3\hat{R}} [a(d_{ij})]^3 - \sqrt{8\pi\sigma\hat{E}} [a(d_{ij})]^3 \right) \vec{e}_{ij}, \quad (2)$$

where the contact radius  $a(d_{ij})$  allows to compute hepatocyte-hepatocyte contact area, and can be obtained by  $d_{ij} = \frac{a^2}{\hat{R}} - \sqrt{\frac{2\pi\sigma}{\hat{E}}}$ ,  $\hat{E}$  and  $\hat{R}$  are defined as  $\hat{E} = \left( \frac{1-\nu_i^2}{E_i} + \frac{1-\nu_j^2}{E_j} \right)^{-1}$  and  $\hat{R} = \left( \frac{1}{R_i} + \frac{1}{R_j} \right)^{-1}$ , with  $E_i$  and  $E_j$  being the Young's moduli,  $\nu_i$  and  $\nu_j$  the Poisson ratios, and  $R_i$  and  $R_j$  the radii of  $i$  and  $j$ . The migration force is computed by  $\vec{F}_{mig,i} = f_{dir} \vec{e}_i + \sqrt{2\Gamma_{ECM,i}^2 D_i} \cdot \vec{\eta}_i$ , where  $f_{dir}$  is one constant force magnitude,  $\vec{e}_i$  is the unit vector from  $i$  towards the central vein,  $D_i$  is the diffusion constant of  $i$ ,  $\vec{\eta}_i$  is an uncorrelated noise term with amplitude  $\langle \eta_{in}(t) \eta_{jm}(t') \rangle = \delta_{ij} \delta_{mn} \delta(t - t')$ ,  $t$  is the time for the current step,  $t'$  is the time for the last step, and  $m, n \in (x, y, z)$  denote the coordinates (see more details in Hoehme et. al., 2010).

**Equation of motion for macrophages (Kupffer cells and infiltrating macrophages) and neutrophils.** Macrophages and neutrophils  $i$  are represented as point objects not interacting with any other structure but capable of migrating along the sinusoids (if not otherwise stated). The position of  $i$  is updated by solving the following equation:

$$\Gamma_{ECM,i} \vec{v}_i + \sum_j \Gamma_{i,j} (\vec{v}_i - \vec{v}_j) = \sum_j \vec{F}_{ij} + \vec{F}_{mig,i}, \quad (3)$$

where  $\Gamma_{ECM,i}$  is the friction coefficient with the extracellular matrix,  $\Gamma_{i,j}$  is the friction tensor between  $i$  and  $j$  (same as Eqn. 1),  $\vec{F}_{ij}$  is the corresponding central repulsion/adhesion interaction force,  $\vec{F}_{mig,i}$  is the migration force to drive  $i$  to migrate. The interaction force in Eqn. (3) does not play an important role as compared to the densely distributed hepatocytes, macrophages and neutrophils are distributed much more sparsely in the lobule, and they are much smaller than hepatocytes.

**Equation of motion for HSCs.** The core body of HSCs is modelled as one homogeneous isotropic, elastic, adhesive sphere (mainly representing the HSC's nucleus) with several semi-flexible chains of spheres as “arms” (to mimic the long HSC's protruding branches). The position of one HSC  $i$  (Fig. S1C) is updated by solving the following equation of motion:

$$\Gamma_{ECM,i}\vec{v}_i + \sum_j \Gamma_{i,j}(\vec{v}_i - \vec{v}_j) = \sum_j \vec{F}_{ij} + \vec{F}_{mig,i} + \sum_k \vec{F}_{ela,ik}, \quad (4)$$

where  $\Gamma_{ECM,i}$  is the friction coefficient with ECM,  $\Gamma_{i,j}$  is the friction tensor between  $i$  and another cell or element  $j$  (same as Eqn. 1),  $\vec{F}_{ij}$  is the interaction force between  $i$  and another cell or element  $j$  (same as Eqn. 2).  $\vec{F}_{ela,ik}$  represents elastic force between the head sphere of  $i$  and its connected arm spheres  $k$  (see definition in Fig. S1C).  $\vec{F}_{mig,i}$  is the migration force to drive  $i$  to migrate. The equation of motion for an arm sphere  $i'$  of HSC  $i$  (blue sphere in Fig. S1C) is approximated by:

$$\Gamma_{ECM,i'}\vec{v}_{i'} = \sum_{k'} \vec{F}_{ela,i'k'}, \quad (4b)$$

where  $k'$  denote the connected spheres of arm sphere  $i'$ . The arms were represented to permit representation of the HSC shape as well as of potential direct cell-cell communication through the arms. However, in reality, these arms are so small that within this work their interaction with other cells was neglected.

**Equation of motion for sinusoids.** Sinusoids are modeled as semi-flexible spheres (Hoehme et al., 2010). For one sinusoid sphere  $i$ , the position of  $i$  is updated by solving the following equation of motion:

$$\Gamma_{ECM,i}\vec{v}_i = \sum_j (\Gamma_{\parallel,SE}(\vec{w}_{ij} - \vec{e}_{ij}(\vec{w}_{ij} \cdot \vec{e}_{ij}))) + \vec{F}_{ij} + \sum_k (\Gamma_{\parallel,SS}(\vec{w}_{ik} - \vec{e}_{ik}(\vec{w}_{ik} \cdot \vec{e}_{ik}))) + \vec{F}_{ik} + \vec{F}_{i,ela}, \quad (5)$$

where  $\Gamma_{ECM,i}$  is the friction coefficient with environment,  $\Gamma_{\parallel,SE}$  denotes the friction between sinusoid sphere  $i$  and its interacting sphere, for example hepatocyte  $j$ ,  $\vec{w}_{ij} = \vec{v}_j - \vec{v}_i$  is the difference of velocity between  $i$  and  $j$ ,  $\vec{e}_{ij}$  is the unit direction vector from  $i$  towards  $j$ ,  $\vec{F}_{ij}$  is the interaction force between  $i$  and  $j$  (same as Eqn. 2),  $\Gamma_{\parallel,SS}$  denotes the friction between two sinusoid spheres  $i$  and  $k$ ,  $\vec{w}_{ik} = \vec{v}_k - \vec{v}_i$  is the difference of velocity between  $i$  and  $k$ ,  $\vec{e}_{ik}$  is the unit direction vector from  $i$  towards  $k$ ,  $\vec{F}_{ik}$  is the interaction force between  $i$  and  $k$ ,  $\vec{F}_{i,ela}$  is the spring force that arises from the chain connections between spheres belonging to the same sinusoid.

### Gradient of signals to regulate cell behaviors

In our model, each type of molecular signal is produced by one type of cell. The dynamic of signal  $i$  released by cell  $j$  is governed by a partial differential equation (PDE):

$$\frac{\partial \phi_i}{\partial t} = \nabla(D_i \nabla \phi_i) + s_i(\sum_j \delta(x - x_j)) - \gamma_i \phi_i, \quad (6)$$

where  $\phi_i$  is the density of  $i$ ,  $D_i$  is the diffusion coefficient of  $i$ ,  $s_i$  is the production rate of  $i$ ,  $x_j$  denotes the position of cell  $j$ , which produces  $i$ ,  $\gamma_i$  is the decay rate of  $i$ . The center of mass of

cell  $j$  is set as the origin of the source. The simulation domain  $\Omega$  is set as a box large enough to contain the entire lobule. The diffusion process of  $i$  inside  $\Omega$  is assumed to be isotropic and homogenous. We assume Dirichlet boundary condition  $\phi_i(x) = 0$  for  $x \in \partial\Omega$ .

**The cubic system to approximate the signal gradient.** We used a simple cubic system to approximate the concentration of all signals. The entire lobule is located in a big cube which is divided into  $N^3$  small element cubes (Fig. S1A,  $N$  is number of element cubes on each axis). The concentration of signal  $l$  at cube  $i, j, k$  at time  $t$  is denoted as  $c_{l:i,j,k}^t$ . After the time lapse of  $\Delta t$ , the concentration is denoted as  $c_{l:i,j,k}^{t+\Delta t}$ . Then the solution of Eqn. 6 can be explicitly approximated as:

$$\frac{c_{l:i,j,k}^{t+\Delta t} - c_{l:i,j,k}^t}{\Delta t} =$$

$$D_l \left( \frac{c_{l:i-1,j,k}^t - 2c_{l:i,j,k}^t + c_{l:i+1,j,k}^t}{\Delta x^2} + \frac{c_{l:i,j-1,k}^t - 2c_{l:i,j,k}^t + c_{l:i,j+1,k}^t}{\Delta y^2} + \frac{c_{l:i,j,k-1}^t - 2c_{l:i,j,k}^t + c_{l:i,j,k+1}^t}{\Delta z^2} \right) + s_l - \gamma_l c_{l:i,j,k}^t,$$

where  $D_l$ ,  $s_l$ ,  $\gamma_l$  are the diffusion coefficient, production rate, and decay rate of  $l$ . Since we use the cube as finite element,  $\Delta x$ ,  $\Delta y$ ,  $\Delta z$  are the same as the width of the element cube. To verify our cubic system, we tested one simple example of placing one injured hepatocyte which produces DAMP in the center of the system. Then we solve Eqn. 6 by using our method and the software deal.II (Arndt et al., 2021) for the numerical solution. As shown in Fig. S1B, our method can get a relatively good approximation of the solution. (We did not use deal.II directly as it turned out to be too slow.)

**Diffusion rate.** In our model, the diffusion rate of one molecule is scaled approximately as the inverse of the cube root of the molecular weight following Goodhill, 1997. We take the diffusion rate of TGF $\beta$ ,  $D_{TGF\beta}$  as reference, the diffusion rate  $D_i$  molecule  $i$  is then approximated as  $D_i = D_{TGF\beta} \left( \frac{w_{TGF\beta}}{w_i} \right)^{1/3}$ , where  $w_{TGF\beta}$  is the molecular weight of TGF $\beta$ ,  $w_i$  is the molecular weight of  $i$ . The diffusion rates of all molecular signals in our model are listed in Table S1.

**Production rate.** The concentrations of above molecules in the in vitro studies in serum or cell are around 1-20 ng/ml (Al-Alwan et al., 2014, De Donat et al., 2008, Gouwy et al., 2009, Jube et al., 2012, Sieber et al., 2018). In our model, the concentration unit of molecule is assumed to be 1 which equals to 5 ng/ml. The production rate  $s_i$  of molecular  $i$  is arbitrarily fixed as 0.1.

**Decay rate.** In our model, the decay rate  $\gamma_i$  of molecule  $i$  is approximated according to its half-life time:  $\gamma_i = \ln 2 / T_{i,1/2}$ , where  $T_{i,1/2}$  is the half-life time of molecule  $i$ . The decay rate of all molecular signals in our model is listed in Table S1.

### Scenario of lobule regeneration

In our model, the cell behaviors are regulated by certain type of signals. Different types of cells communicated with each other by responding to specific signals and collaborated to achieve the clearance of necrotic region and recovery from the toxin-induced injury.

**Behaviors of hepatocytes.** We assume that the hepatocytes within  $164\ \mu\text{m}$  (the lobule lesion size due to  $\text{CCl}_4$ -induced injury is taken from Hoehme et al., 2010) from the central vein of the lobule are  $\text{CCl}_4$ -induced injured cells. In our model, they are marked as *injured* hepatocytes, which can synthesize DAMPs (Li et al., 2020, Calderwood et al., 2016) to activate, among others, Kupffer cells and infiltrating macrophages (Martin-Murphy et al., 2010, Mihm, 2018). Activated Kupffer cells and activated HSCs can produce CXCL1 to attract neutrophils to migrate into the lesion area (Marra and Tacke, 2014), and CCL2 to attract infiltrating macrophages.

We have observed that the majority of the hepatocytes are dead 2 hours after the administration of APAP in vitro (experimental data not shown here). A previous study also showed that neutrophils can induce necrosis of hepatocytes upon administration of APAP (Marques et al., 2012). In our model, we assigned random waiting times for each *injured* hepatocyte  $i$  according to one Gamma distribution  $\text{Gamma}(\alpha = 5, \beta = 5)$ . After the waiting time is up,  $i$  is marked as *dead (necrotic)* hepatocyte. The choice of  $\alpha$  is because the necrotic pathway triggered for hepatocytes due to AILI (acetaminophen-induced liver injury) involves about 5 reactions (Dichamp et al., manuscript in preparation) and the choice of  $\beta$  is to fit the data that almost all hepatocytes are dead 2 hours after the administration of APAP. In addition to APAP, neutrophils can also induce necrosis of hepatocytes. For any *injured* hepatocyte  $i$ , if its distance with one neutrophil  $j$  satisfies  $d_{ij} < r_i + r_j$ , it is then marked as *dead (necrotic)* hepatocyte (neutrophil can evoke the necrosis of a hepatocyte, Marra and Tacke, 2014). We assumed that for any dead hepatocyte  $i$  enduring for more than 24 hours, it then can be eliminated by macrophages (it takes roughly 24 hours for a dying cell to lose its membrane integrity and collapse into fragments, Maruyama et al., 2001). Since it usually takes 2-4 hours for one macrophage to engulf and degrade foreign objects such as dead cell bodies (Haecker et al., 2002), we simulate the degradation process of one dead body of hepatocyte  $i$  if it gets contact with one Kupffer cell or infiltrating macrophage  $j$  with Ly6C-high phenotype, such that the distance between them satisfies  $d_{ij} < r_i + r_j$ ,  $i$  is removed from the model system, 3 hours after the contact.

**Behaviors of Kupffer cells.** We assume that for one Kupffer cell  $i$ , if its local concentration of DAMP,  $\phi_{\text{DAMP},i}$  is higher than a threshold  $\phi_{\text{DAMP},\text{activate}}$ ,  $i$  is activated and can synthesize TGF $\beta$ , CXCL1, CCL2, and PDGF (Pinzani et al., 1994, De Bleser et al., 1997, Marra and Tacke, 2014, Krenkel et al., 2014). A previous study has reported that due to its highly stationary behavior, Kupffer cells "are not suited" to migrate to the injury site (Ju and Tacke, 2016), but the presence of HSCs does promote the migration of Kupffer cells towards HSCs (Seki et al., 2007). We assume that one activated Kupffer cell  $i$  can migrate towards one activated HSC  $j$  if the distance between them satisfies  $d_{ij} < r_i + r_j + l_{\text{HSC},\text{branch}}$ , where  $l_{\text{HSC},\text{branch}}$  is the length of the HSC branch. A migration force  $\vec{F}_{\text{mig},i} = f_{\text{mig},i} \frac{\vec{e}_{ij}}{\|\vec{e}_{ij}\|}$ ,  $f_{\text{mig},i} \sim \mathcal{N}(F_{\text{mig},\text{KC},\text{mean}}, F_{\text{mig},\text{KC},\text{sd}})$  on  $i$  is then added to the equation of motion of cell  $i$ , where  $\vec{e}_{ij}$  is the orientation unit vector from  $i$  to  $j$ ,  $F_{\text{mig},\text{KC},\text{mean}}$  and  $F_{\text{mig},\text{KC},\text{sd}}$  are the mean and standard deviation of migration force magnitude approximated from the mean and standard deviation of migration speed of Kupffer cells (due to the highly stationary behavior of Kupffer cells (Ju and Tacke, 2016), we arbitrarily set a low migration speed for them. We also tested higher and even lower migration speed of

Kupffer cells in Fig. S3) as  $F_{mig,KC,mean} = \Gamma_{ECM,KC} v_{KC,mean}$ ,  $F_{mig,KC,sd} = \Gamma_{ECM,KC} v_{KC,sd}$  (see value of  $v_{KC,mean}$  and  $v_{KC,sd}$  in Table S1). Since dead hepatocytes can be engulfed by Kupffer cells (Canbay et al., 2003) and the phagocytosis ability of macrophages is decreased by 50% after it uptakes dead cells (Erwig et al., 1999), we assigned one phagocytosis probability  $p_{phag,i}$  for each activated Kupffer cell  $i$ , where  $p_{phag,i}$  is initiated as 1. If the distance between  $i$  and one dead hepatocyte  $j$  satisfies  $d_{ij} < r_i + r_j$ , and one random number sampled from uniform distribution  $U(0,1)$  is less than  $p_{phag,i}$ , then  $i$  stops moving and remains with hepatocyte  $j$  for 3 hours to engulf and degrade the dead hepatocyte.  $p_{phag,i}$  is then divided by two to mimic the decreased phagocytosis ability of  $i$ . If there are more than one dead hepatocyte in contact with  $i$ , only one of them is randomly selected as the one to be engulfed by  $i$ . After 3 hours,  $j$  is removed from the system and  $i$  can move again. In our model, we consider two alternative time courses for Kupffer cells. Either their population size drops upon activation, recovering from day 2 on, or the Kupffer cell population remains constant. Since in the latter case the life span of one Kupffer cell is no longer than about 4 days, as reported in Naito et al., 2004, we assume that each Kupffer cell would revert to a quiescent mode after it is activated.

**Behaviors of HSCs.** PDGF has been reported to attract HSCs to migrate (Melton and Yee, 2007, Yang et al., 2003). We assume that for one HSC  $i$ , if its local concentration of PDGF,  $\phi_{PDGF,i}$  is higher than a threshold  $\phi_{PDGF,migrate}$ , a migration force  $\vec{F}_{mig,i} = f_{mig,i} \frac{\nabla \phi_{PDGF,i}}{\|\nabla \phi_{PDGF,i}\|}$ ,  $f_{mig,i} \sim \mathcal{N}(F_{mig,HSC,mean}, F_{mig,HSC,sd})$  is then applied on  $i$ , where  $F_{mig,HSC,mean}$  and  $F_{mig,HSC,sd}$  are the mean and standard deviation of migration force magnitude approximated from the mean and standard deviation of migration speed of HSC (Tangkijvanich et al., 2001) as  $F_{mig,HSC,mean} = \Gamma_{ECM,HSC} v_{HSC,mean}$ ,  $F_{mig,HSC,sd} = \Gamma_{ECM,HSC} v_{HSC,sd}$  (see value of  $v_{HSC,mean}$ ,  $v_{HSC,sd}$  in table S1). Every HSC is initiated as in *quiescent* mode. TGF $\beta$  has been reported to activate HSCs, but it was also suggested that it is not TGF $\beta$  but one factor produced by infiltrating macrophages that activates HSCs (Imamura et al., 2005). Here we assume two alternative mechanisms for HSC activation. One is that HSCs are activated by TGF $\beta$  produced by Kupffer cells. If the local concentration of TGF $\beta$ ,  $\phi_{TGF\beta,i}$  at HSC  $i$  is higher than a threshold  $\phi_{TGF\beta,activate}$ ,  $i$  is activated into the *activated* mode; the other is that HSCs are activated by one factor produced by infiltrating macrophages (the type of this factor is not known, so we assume it has the same diffusion constant and decay rate of TGF $\beta$ ). If the local concentration of this factor,  $\phi_{factor,i}$  at HSC  $i$  is higher than the threshold  $\phi_{TGF\beta,activate}$ ,  $i$  is activated into *activated* mode. Upon activation, HSCs can synthesize CXCL1 and CCL2 (Kisseleva and Brenner, 2007, Baeck et al., 2012). HSCs remain activated even if TGF $\beta$  falls below the threshold again. As reported before, activated HSCs are phagocytosed by Ly6C-low phenotype infiltrating macrophages in the later stage of liver regeneration (Tacker and Zimmermann, 2014) (mechanism 1). In addition to phagocytosis, we assumed another mechanism (mechanism 2) for the fate of activated HSCs: Ly6C-low phenotype infiltrating macrophages can revert activated HSCs to the quiescent mode. In our model, these two mechanisms are simulated as following: if hepatocyte  $i$  is in activated mode,  $d_{ij} < r_i + r_j$  it is eliminated under mechanism 1) or reverted to quiescent mode again under mechanism 2). To keep the same density of HSCs after liver regeneration, we assumed that under mechanism 1), once  $i$  is activated, it grows and divides after 24 hours.



**Behaviors of infiltrating macrophages.** DAMPs are suggested to activate macrophages (Mihm 2018). We assume that for one infiltrating macrophage  $i$ , if its local concentration of DAMP,  $\phi_{DAMP,i}$  is higher than a threshold  $\phi_{DAMP,activate}$ ,  $i$  is activated and can synthesize CCL2, and PDGF (Baeck et al., 2012, Pinzani et al., 1994). During liver regeneration, macrophages infiltrate into the liver following the chemoattract of CCL2 (Baeck et al., 2012). We assume that for one infiltrating macrophage  $i$ , if its local concentration of CCL2,  $\phi_{CCL2,i}$  is higher than a threshold  $\phi_{CCL2,migrate}$ , a migration force  $\vec{F}_{mig,i} = f_{mig,i} \frac{\nabla \phi_{CCL2,i}}{\|\nabla \phi_{CCL2,i}\|}$ ,  $f_{mig,i} \sim \mathcal{N}(F_{mig,IM,mean}, F_{mig,IM,sd})$  is then applied on  $i$ , where  $F_{mig,IM,mean}$  and  $F_{mig,IM,sd}$  are the mean and standard deviation of the migration force magnitude, approximated from the mean and standard deviation of migration speed of infiltrating macrophages (Grabher et al., 2007) as  $F_{mig,IM,mean} = \Gamma_{ECM,IM} v_{IM,mean}$ ,  $F_{mig,IM,sd} = \Gamma_{ECM,IM} v_{IM,sd}$  (see value of  $v_{IM,mean}$ ,  $v_{IM,sd}$  in Table S1). Each infiltrating macrophage is initiated as Ly6C-high phenotype, which is responsible of degrading necrotic cells (Tacke and Zimmermann, 2014). After a certain duration it transforms into Ly6C-low phenotype, which is responsible of anti-fibrosis (Ramachandran et al., 2012, Tacke and Zimmermann, 2014). If the distance between one infiltrating macrophage  $i$  in Ly6C-high phenotype and one dead hepatocyte  $j$  satisfies  $d_{ij} < r_i + r_j$ ,  $j$  is removed 3 hours later to mimic the process of engulfment and degradation of apoptotic hepatocytes (Boulter et al., 2012). There is also the same phagocytose probability  $p_{phag,i}$  assigned to  $i$  to mimic the decreased phagocytosis ability of the macrophage (Erwig et al., 1999). If the distance between one infiltrating macrophage  $i$  in Ly6C-low phenotype and one activated HSC  $j$  satisfies  $d_{ij} < r_i + r_j$ , and one random number sampled from  $U(0,1)$  is less than  $p_{phag,i}$ ,  $j$  is removed or reverted to quiescent mode under mechanisms 1) and 2) of the fate of activated HSC, respectively. If mechanism 1) is used,  $p_{phag,i}$  is then halved. The infiltrating macrophages are initiated as monocytes with Ly6C-high phenotype, and after a period of time between 2 and 3 days they transform into macrophages with Ly6C-low phenotype (Zigmond et al., 2014, Graubardt et al., 2017). The transforming time from Ly6C-high phenotype to Ly6C-low phenotype is chosen as 72 hours according to the observation from Zigmond et al., 2014 (the mass peak of Ly6C-low phenotype macrophages is at 3 days after the injury). The Ly6C-high phenotype may not be stained by F4/80 (as shown in Fig. 2 of Dragomir et al., 2012). Hence, at day 2 after the injury, F4/80 staining shows only the Ly6C-low phenotype, which are the KCs (Fig. 1A). The lifetime of one infiltrating macrophage in the system is set to be 96 hours (estimated from the observation from the APAP-induced liver injury done by Zigmond et al., 2014, where the mass peak of infiltrating macrophages is at 1 day after the injury and they are hardly to be seen 5 days after the injury). Infiltrating macrophages are added into the lobule system evenly during the first 24 hours. The initial position of one infiltrating macrophage is randomly sampled inside the lobule but outside of the lesion (164  $\mu\text{m}$  away from the central vein) reflecting their approximate distribution at the time when they start to migrate on response to CCL2, whose peak is at about day 1.

**Behaviors of neutrophils.** Neutrophils are recruited by CXCL1 at the early stage of liver injury (De Filippo et al., 2013). We assume that for one neutrophil  $i$ , if its local concentration of CXCL1,  $\phi_{CXCL1,i}$  is higher than a threshold  $\phi_{CXCL1,migrate}$ , a migration force  $\vec{F}_{mig,i} =$

$f_{mig,i} \frac{\nabla \phi_{CXCL1,i}}{\|\nabla \phi_{CXCL1,i}\|}, f_{mig,i} \sim \mathcal{N}(F_{mig,Neutrophil,mean}, F_{mig,Neutrophil,sd})$  is then applied on  $i$ ,  
 $F_{mig,Neutrophil,mean}$  and  $F_{mig,Neutrophil,sd}$  are the mean and standard deviation of the  
migration force magnitude, approximated from the mean and standard deviation of migration  
speed of neutrophils (Marques et al., 2014) as  
 $F_{mig,Neutrophil,mean} = \Gamma_{ECM,Neutrophil} v_{Neutrophil,mean}$ ,  
 $F_{mig,Neutrophil,sd} = \Gamma_{ECM,Neutrophil} v_{Neutrophil,sd}$  (see value of  $v_{Neutrophil,mean}$ ,  $v_{Neutrophil,sd}$  in  
Table S1). If its distance with one injured hepatocyte  $j$  satisfies  $d_{ij} < r_i + r_j$ ,  $j$  is then marked as  
a dead (necrotic) hepatocyte (neutrophils induce the necrosis of hepatocytes during acute liver  
injury, Ramaiah and Jaeschke, 2007). The lifetime of one neutrophil in the system is set to be 48  
hours (Graubardt et al., 2017). Neutrophils are added into the lobule system evenly during the  
first 24 hours. They migrate very quick. In the model, the initial position of each neutrophil is  
randomly sampled inside the lobule but outside of the lesion (164  $\mu\text{m}$  away from the central  
vein).

**Behaviors of platelets/sinusoids.** Following liver injury, platelets are recruited to the liver and  
adhere to the endothelium to generate factors such as PDGF and HGF (Meyer et al., 2015,  
Nowatari et al., 2014). In our model, platelets are not explicitly modeled. The sinusoid spheres  
within the lesion ( $< 164 \mu\text{m}$  away from the central vein) are considered as endothelium  
adherent with platelets, which are an additional source of PDGF. The presence of platelet-  
adherent sinusoid spheres lasts until day 2 (the count of platelets resumes to normal after day  
2, as reported in Stravitz et al., 2017). The promotive effect of platelet released HGF on the  
proliferation of hepatocytes is not modeled explicitly. The proliferation of hepatocytes is  
modeled by applying a spatio-temporal proliferation pattern extracted from experimental data  
on all healthy hepatocytes in the liver according to its location and time (Hoehme et al., 2010).

**Dynamic of signals.** In our model, DAMPs are synthesized by injured and dead hepatocytes;  
TGF $\beta$  is synthesized by activated Kupffer cells; CCL2 is synthesized by activated Kupffer cells,  
activated HSCs, activated infiltrating macrophages, and platelet-adherent sinusoids; CXCL1 is  
synthesized by activated Kupffer cells and activated HSCs; PDGF is synthesized by platelet-  
adherent sinusoids and Kupffer cells. There is also one factor synthesized by activated  
infiltrating macrophages. We assume that this factor takes the same diffusion coefficient and  
decay rate as TGF $\beta$ . The simulated sensitivity test of the concentration of each signal to  
regulate the behavior of a certain cell type is shown in Fig. S3. The production rate coefficient  
for TGF $\beta$  is multiplied by 5 when its source cell, Kupffer cell is phagocytosing dead hepatocytes,  
by taking into account the observation that the TGF $\beta$  expression level in Kupffer cells incubated  
with apoptotic cells is 5-fold higher than those incubated without apoptotic cells (Canbay et al.,  
2003).

## REFERENCES

Al-Alwan, L.A., Chang, Y., Rousseau, S., Martin, J.G., Eidelman, D.H., Hamid, Q. (2014). CXCL1  
inhibits airway smooth muscle cell migration through the decoy receptor duffy antigen receptor  
for chemokines. The Journal of Immunology 193, 1416—1426.

1038 Amiri, K.I., Richmond, A. (2003). Fine tuning the transcriptional regulation of the CXCL1  
1039 chemokine. *Progress in Nucleic Acid Research and Molecular Biology* 74, 1—36.

1040 Baeck, C., Wehr, A., Karlmark, K.R., Heymann, F., Vucur, M., Gassler, N., Huss, S., Klussmann, S.,  
1041 Eulberg, D., Luedde, T., Trautwein, C., Tacke, F. (2012). Pharmacological inhibition of the  
1042 chemokine CCL2 (MCP-1) diminishes liver macrophage infiltration and steatohepatitis in chronic  
1043 hepatic injury. *Gut* 61(3), 416—426.

1044 Berchiche, Y.A., Gravel, S., Pelletier, M., St-Onge, G., Heveker, N. (2011). Different effects of the  
1045 different natural CC chemokine receptor 2b ligands on  $\beta$ -arrestin recruitment, G $\alpha$ i signaling,  
1046 and receptor internalization. *Molecular Pharmacology* 79(3), 488—498.

1047 Boulter, L., Govaere, O., Bird, T.G., Radulescu, S., Ramachandran, P., Pellicoro, A., Ridgway, R.A.,  
1048 Seo, S.S., Spee, B., Van Rooijen, N., Sansom, O.J., Iredale, J.P., Lowell, S., Roskams, T., Forbes,  
1049 S.J. (2012). Macrophage derived Wnt signaling opposes Notch signalling in a Numb mediated  
1050 manner to specify HPC fate in chronic liver disease in human and mouse. *Nature Medicine* 18,  
1051 572—579.

1052 Bouwens, L., Knook, D.L., Wisse, E. (1986). Local proliferation and extrahepatic recruitment of  
1053 liver macrophages (Kupffer cells) in partial-body irradiated rats. *Journal of Leukocyte Biology*  
1054 39, 687—697.

1055 Brenner, C., Galluzzi, L., Kepp, O., Kroemer, G. (2013). Decoding cell death signals in liver  
1056 inflammation. *Journal of Hepatology* 59, 583—594.

1057 Bufi, N., Saitakis, M., Dogniaux, S., Buschinger, O., Bohineust, A., Richert, A., Maurin, M., Hivroz,  
1058 C., Asnacios, A. (2015). Human primary immune cells exhibit distinct mechanical properties that  
1059 are modified by inflammation. *Biophysical Journal* 108(9), 2181—2190.

1060 Cai, X., Li, Z., Zhang, Q., Qu, Y., Xu, M., Wan, X., Lu, L. (2018). CXCL-EGFR-induced kupffer cells  
1061 secrete TGF- $\beta$ 1 promoting hepatic stellate cell activation via the SMAD2/BRD4/C-MYC/EZH2  
1062 pathway in liver fibrosis. *Journal of Cellular and Molecular Medicine* 22, 5050—5061.

1063 Calderwood, S.K., Gong, J., Murshid, A. (2016). Extracellular HSPs: the complicated roles of  
1064 extracellular HSPs in immunity. *Frontiers in Immunology* 7, 159.

1065 Campos, G., Schmidt-Heck, W., De Smedt, J., Widera, A., Ghallab, A., Putter, L., et al. (2020).  
1066 Inflammation-associated suppression of metabolic gene networks in acute and chronic liver  
1067 disease. *Arch. Toxicol.* 94, 205—217.

1068 Canbay, A., Feldstein, A.E., Higuchi, H., Werneburg, N., Grambihler, A., Bronk, S.F., Gores, G.J.  
1069 (2003). Kupffer cell engulfment of apoptotic bodies stimulates death ligand and cytokine  
1070 expression. *Hepatology* 38(5), 1188—1198.

1071 Chu, Y., Dufour, S., Thiery, J.P., Perez, E., Pincet, F. (2005). Johnson-Kendall-Roberts theory  
1072 applied to living cells. *Physical Review Letters* 94(2): 028102.

1073 Davies, J.E., Apta, B.H.R., Harper, M.T. (2018). Cross-reactivity of anti-HMGB1 antibodies for  
1074 HMGB2. *Journal of Immunological Methods* 456, 72—76.

1075 De Bleser, P.J., Niki, T., Rogiers, V., Geerts, A. (1997). Transforming growth factor- $\beta$  gene  
1076 expression in normal and fibrotic rat liver. *Journal of Hepatology* 26(4), 886—893.

1077 De Donatis, A., Comito, G., Buricchi, F., Vinci, M.C., Parenti, A., Caselli, A., Camici, G., Manao, G.,  
1078 Ramponi, G., Cirri, P. (2008). Proliferation versus migration in platelet-derived growth factor  
1079 signaling. *The Journal of Biological Chemistry* 283(29), 19948—19956.

1080 De Filippo, K., Dudeck, A., Hasenberg, M., Nye, E., Van Rooijen, N., Hartmann, K., Gunzer, M.,  
1081 Roers, A., Hogg, N. (2013). Mast cell and macrophage chemokines CXCL1/CXCL2 control the  
1082 early stage of neutrophil recruitment during tissue inflammation. *Blood* 121(24), 4930—4937.

1083 Drasdo, D., Hoehme, S., Hengstler, J.G. (2014). How predictive quantitative modelling of tissue  
1084 organisation can inform liver disease pathogenesis. *Journal of Hepatology* 61(4), 951—956.

1085 Dragomir, A.D., Sun, R., Choi, H., Laskin, J.D., Laskin, D.L. (2012). Role of Galectin-3 in classical  
1086 and alternative macrophage activation in the liver following acetaminophen intoxication. *The*  
1087 *Journal of Immunology* 189, 5934—5941.

1088 Dutta-Moscato, J., Solovyev, A., Mi, Q., Nishikawa, T., Soto-Gutierrez, A., Fox, I.J., Vodovotz, Y.  
1089 (2014). A multiscale agent-based in silico model of liver fibrosis progression. *Frontiers in*  
1090 *Bioengineering and Biotechnology* 2, 18.

1091 Erwig, L., Gordon, S., Walsh, G.M., Rees, A.J. (1999). Previous uptake of apoptotic neutrophils or  
1092 ligation of integrin receptors downmodulates the ability of macrophages to ingest apoptotic  
1093 neutrophils. *Blood* 93(4), 1406—1412.

1094 Fan, W., Liu, T., Chen, W., Hammad, S., Longerich, T., Hausser, I., Fu, Y., Li, N., He, Y., Liu, C.,  
1095 Zhang, Y., Lian, Q., Zhao, X., Yan, C., Li, L., Yi, C., Ling, Z., Ma, L., Zhao, X., Xu, H., Wang, P., Cong,  
1096 M., You, H., Liu, Z., Wang, Y., Chen, J., Li, D., Hui, L., Dooley, S., Hou, J., Jia, J., Sun, B. (2019).  
1097 ECM1 prevents activation of transforming growth factor  $\beta$ , hepatic stellate cells, and  
1098 fibrogenesis in mice. *Gastroenterology* 157(5), 1352—1367.

1099 Fischer, R., Cariers, A., Reinehr, R., Häussinger, D. (2002). Caspase 9-dependent killing of  
1100 Hepatic Stellate Cells by activated Kupffer cells. *Gastroenterology* 123, 845—861.

1101 Friedman, A., Hao, W. (2017). Mathematical modeling of liver fibrosis. *Mathematical*  
1102 *Biosciences and Engineering* 14(1), 143—164.

1103 Gao, B., Radaeva, S. (2013). Natural killer and natural killer T cells in liver fibrosis. *Biochimica et*  
1104 *Biophysica Acta – Molecular Basis of Disease* 1832(7), 1061—1069.

1105 Gardin, I., Linhart, N.C., Petiet, A., Bok, B. (1992). Dosimetry at the cellular level of Kupffer cells  
1106 after technetium-99m-sulphur colloid injection. *The Journal of Nuclear Medicine* 33(2), 380—  
1107 384

1108 Ghallab, A., Celliere, G., Henkel, S.G., Driesch, D., Hoehme, S., Hofmann, U., Zellmer, S., Godoy,  
1109 P., Sachinidis, A., Blaszkewicz, M., et al. (2016). Model-guided identification of a therapeutic  
1110 strategy to reduce hyperammonemia in liver diseases. *Journal of Hepatology* 64(4), 860—871.

1111 Ghallab, A., Myllys, M., Holland, C.H., Zaza, A., Murad, W., Hassan, R., Ahmed, Y.A., Abbas, T.,  
1112 Abdelrahim, E.A., Schneider, K.M., Matz-Soja, M., Reinders, J., Gebhardt, R., Berres, M., Hatting,  
1113 M., Drasdo, D., Saez-Rodriguez, J., Trautwein, C., Hengstler, J.G. (2019). Influence of liver  
1114 fibrosis on lobular zonation. *Cells* 8(12), 1556.

1115 Ghallab, A., Myllys, M., Friebe, A., Duda, J., Edlund, K., Halilbasic, E., Vucur, m., Hobloss, Z.,  
1116 Brackhagen, L., Begher-Tibbe, B., et al. (2021). Spatio-Temporal Multiscale Analysis of Western  
1117 Diet-Fed Mice Reveals a Translationally Relevant Sequence of Events during NAFLD Progression.  
1118 *Cells* 10(10), 2516.

1119 Ghallab, A., Hassan, R., Hofmann, U., Friebe, A., Hobloss, Z., Brackhagen, L., Begher-Tibbe, B.,  
1120 Myllys, M., Reinders, J., Overbeck, N., Sezgin, S., Zühlke, S., Seddek, A., Murad, W.,  
1121 Brecklinghaus, T., Kappenberg, F., Rahnenführer, J., González, D., Goldring, C., Copple, I.,  
1122 Marchan, R., Longerich, T., Vucur, M., Luedde, T., Urban, S., Canbay, A., Schreiter, T., Trauner,  
1123 M., Akakpo, J., Olyae, M., Curry, S., Sowa, J., Jaeschke, H., Hoehme, S., Hengstler, J.G. (2022).  
1124 Interruption of bile acid uptake by hepatocytes after acetaminophen overdose ameliorates  
1125 hepatotoxicity. *Journal of Hepatology*, accepted in press.

1126 Gianmoena, K., Gasparoni, H., Jashari, A., Gabrys, P., Grgas, K., Ghallab, A., et al. (2021).  
1127 Epigenomic and transcriptional profiling identifies impaired glyoxylate detoxification in NAFLD  
1128 as a risk factor for hyperoxaluria. *Cell Reports* 36, 109526.

1129 Goodhill, G.J. (1997). Diffusion in axon guidance. *European Journal of Neuroscience* 9, 1414—  
1130 1421.

1131 Gouwy, M., Struyf, S., Verbeke, H., Put, W., Proost, P., Opdenakker, G., Van Damme, J. (2009).  
1132 CC chemokine ligand-2 synergizes with the nonchemokine G protein-coupled receptor ligand  
1133 fMLP in monocyte chemotaxis, and it cooperates with the TLR ligand LPS via induction of CXCL8.  
1134 *Journal of Leukocyte Biology* 86, 671—680.

1135 Grabher, C., Cliffe, A., Miura, K., Hayflick, J., Pepperkik, R., Rørth, P., Wittbrodt, J. (2007). Birth  
1136 and life of tissue macrophages and their migration in embryogenesis and inflammation in  
1137 medaka. *Journal of Leukocyte Biology* 81(1), 263—271.

1138 Graubardt, N., Vugman, M., Mouhadeb, O., Caliri, G., Pasmanik-Chor, M., Reuveni, D.,  
1139 Zigmond, E., Brazowski, E., David, E., Chappell-Maor, L., Jung, S., Varol, C. (2017). Ly6Chi  
1140 monocytes and their macrophage descendants regulate neutrophil function and clearance in  
1141 acetaminophen-induced liver injury. *Frontiers in Immunology* 8, 626.

1142 Haecker, H., Fuermann, C., Wagner, H., Haecker, G. (2002). Caspase-9/-3 activation and  
1143 apoptosis are induced in mouse macrophages upon ingestion and digestion of *Escherichia coli*  
1144 bacteria. *The Journal of Immunology* 169, 3172—3179.

1145 Hassan, R. (2017). Mechanisms of activated hepatic stellate cell removal in acute and chronic  
1146 liver injury. Thesis, Justus-Liebig-Universität Giessen.

1147 Herant, M., Heinrich, V., Dembo, M. (2005). Mechanics of neutrophil phagocytosis: behavior of  
1148 the cortical tension. *Journal of Cell Science* 118, 1789—1797.

1149 Hetherington, J., Sumner, T., Seymour, R.M., Li, L., Rey, M.V., Yamaji, S., Saffrey, P.,  
1150 Margoninski, O., Bogle, I.D.L., Finkelstein, A., Warner, A. (2012). A composite computational  
1151 model of liver glucose homeostasis. I. building the composite model. *Journal of the Royal*  
1152 *Society Interface* 9, 689—700.

1153 Ho, H., Yu, H.B., Bartlett, A., Hunter, P. (2020). An in silico pipeline for subject-specific  
1154 hemodynamics analysis in liver surgery planning. *Computer Methods in Biomechanics and*  
1155 *Biomedical Engineering* 23(4), 138—142.

1156 Ho, H., Dahmen, U., Hunter, P. (2020a). An in silico rat liver atlas. *Computer Methods in*  
1157 *Biomechanics and Biomedical Engineering* 23(10), 597—600.

1158 Hoehme, S., Hengstler, J.G., Brulport, M., Schaefer, M., Bauer, A., Gebhardt, R., Drasdo, D.  
1159 (2007). Mathematical modelling of liver regeneration after intoxication with CCl<sub>4</sub>. *Chemico-*  
1160 *Biological Interactions* 168(1): 74—93.

1161 Hoehme, S., Drasdo, D. (2010). A cell-based simulation software for multi-cellular systems.  
1162 *Bioinformatics* 26(20), 2641—2642.

1163 Hoehme, S., Brulport, M., Bauer, A., Bedawy, E., Schormann, W., Hermes, M., Puppe, V.,  
1164 Gebhardt, R., Zellmer, S., Schwarz, M., Bockamp, E., Timmel, T., Hengstler, J.G., Drasdo, D.  
1165 (2010). Prediction and validation of cell alignment along microvessels as order principle to  
1166 restore tissue architecture in liver regeneration. *Proceedings of the National Academy of*  
1167 *Sciences* 107(23), 10371—10376.

1168 Hoehme, S., Boettger, J., Hammad, S., Begher-Tibbe, B., Bucur, P., Vibert, E., Gebhardt, R.,  
1169 Hengstler, J.G., Drasdo, D. (2022). A predictive computational model shows that biomechanical  
1170 cell cycle progresion control can explain liver regeneration after partial hepatectomy. Accepted.

1171 Holland, C.H., Ramirez, F., Myllys, M., Hassan, R., Edlund, K., Hofman, U., et al. (2022).  
1172 Transcriptomic cross-species analysis of chronic liver disease reveals consistent regulation  
1173 between humans and mice. *Hepatol. Commun.* 6, 161—177.

1174 Huebener, P., Hernandez, C., Schwabe, R.F. (2015). HMGB1 and injury amplification. *Oncotarget*  
1175 6(27), 23048—23049.

1176 Imamura, M., Ogawa, T., Sasaguri, Y., Chayama, K., Ueno, H. (2005). Suppression of macrophage  
1177 infiltration inhibits activation of hepatic stellate cells and liver fibrogenesis in rats.  
1178 *Gastroenterology* 128(1), 138—146.

1179 Jagiella, N., Rickert, D., Theis, F.J., Hasenauer, J. (2017). Parallelization and high-performance  
1180 computing enables automated statistical inference of multi-scale models. *Cell Systems* 4(2),  
1181 194—206.

1182 Jerby, L., Shlomi, T., Ruppin, E. (2010). Computational reconstruction of tissue-specific  
1183 metabolic models: application to human liver metabolism. *Molecular Systems Biology* 6, 401.

1184 Jikine, A., Edelstein-Keshet, L. (2011). A comparison of mathematical models for polarization of  
1185 single eukaryotic cells in response to guided cues. *PLoS Computational Biology* 7(4), e1001121.

1186 Ju, C., Tacke, F. (2016) Hepatic macrophages in homeostasis and liver diseases: from  
1187 pathogenesis to novel therapeutic strategies. *Cellular & Molecular Immunology* 13(3), 316—  
1188 327.

1189 Jube, S., Rivera, Z., Bianchi, M.E., Powers, A., Wang, E., Pagano, I., Pass, H.I., Gaudino, G.,  
1190 Carbone, M., Yang, H. (2012). Cancer cell secretion of the DAMP protein HMGB1 supports  
1191 progression in malignant mesothelioma. *Cancer Research* 72(13), 3290—3301.

1192 Kang, L., Mars, W.M., Michalopoulos, G.K. (2012). Signals and cells involved in regulating liver  
1193 regeneration. *Cells* 1(4), 1261—1292.

1194 Kim, M., Silberberg, Y., Abeyaratne, R., Kamm, R.D., Asada, H.H. (2018). Computational  
1195 modeling of three-dimensional ECM-rigidity sensing to guide directed cell migration.  
1196 *Proceedings of the National Academy of Sciences* 115(3), E390—E399.

1197 Kisseleva, T., Brenner, D.A. (2007). Role of hepatic stellate cells in fibrogenesis and the reversal  
1198 of fibrosis. *Journal of Gastroenterology and Hepatology* 22, 573—578.

1199 Kisseleva, T., Cong, M., Paik, Y., Scholten, D., Jiang, C., Benner, C., Iwaisako, K., Moore-Morris,  
1200 T., Scott, B., Tsukamoto, H., et al. (2012). Myofibroblasts revert to an inactive phenotype during  
1201 regression of liver fibrosis. *Proceedings of the National Academy of Sciences* 109(24), 9448—  
1202 9453.

1203 Kisseleva, T., Brenner, D. (2021). Molecular and cellular mechanisms of liver fibrosis and its  
1204 regression. *Nature Reviews Gastroenterology & Hepatology* 18, 151—166.

1205 Knutsdottir, H., Zmurchok, C., Bhaskar, D., Palsson, E., Nogare, D.D., Chitnis, A.B., Edelstein-  
1206 Keshet, L. (2017). Polarization and migration in the zebrafish posterior lateral line system. *PLoS*  
1207 *Computational Biology* 13(4), e1005451.

1208 Krenkel, O., Mossanen, J.C., Tacke, F. (2014). Immune mechanisms in acetaminophen-induced  
1209 acute liver failure. *Hepatobiliary Surgery & Nutrition* 3(6), 331—343.

1210 Kuepfer, L., Clayton, O., Thiel, C., Cordes, H., Nudischer, R., Blank, L.M., Baier, V., Heymans, S.,  
1211 Caiment, F., Roth, A., Fluri, D.A., Kelm, J.M., Castell, J., Selevsek, N., Schlapbach, R., Keun, H.,  
1212 Hynes, J., Sarkans, U., Gmuender, H., Herwig, R., Niederer, S., Schuchhardt, J., Segall, M.,

1213 Kleinjans, J. (2018). A model-based assay design to reproduce in vivo patterns of acute drug-  
1214 induced toxicity. *Archives of Toxicology* 92(1), 553—555.

1215 Lambers, L., Suditsch, M., Wagner, A., Ricken, T. (2021). A multiscale and multiphase model of  
1216 function-perfusion growth processes in the human liver. *Proceedings in Applied Mathematics*  
1217 *and Mechanics* 20(1), e20200290.

1218 Lee, Y., Patel, D., Park, S. (2011). Local rheology of human neutrophils investigated using atomic  
1219 force microscopy. *International Journal of Biological Sciences* 7(1), 102—111.

1220 Leist, M., Ghallab, A., Graepel, R., et al. (2017). Adverse outcome pathways: opportunities,  
1221 limitations and open questions. *Archives of Toxicology* 91: 3477—3505.

1222 Li, H., Zhou, Y., Wang, H., Zhang, M., Qiu, P., Zhang, M., Zhang, R., Zhao, Q., Liu, J. (2020).  
1223 Crosstalk between liver macrophages and surrounding cells in nonalcoholic steatohepatitis.  
1224 *Frontiers in Immunology* 11, 1169.

1225 Liu, Z., Govindarajan, S., Kaplowitz, N. (2004). Innate immune system plays a critical role in  
1226 determining the progression and severity of acetaminophen hepatotoxicity. *Gastroenterology*  
1227 127, 1760—1774.

1228 Liu, Z., Han, D., Gunawan, B., Kaplowitz, N. (2006). Neutrophil depletion protects against murine  
1229 acetaminophen hepatotoxicity. *Hepatology* 43(6), 1220—1230.

1230 Marques, P.E., Amaral, S.S., Pires, D.A., Nogueira, L.L., Soriani, F.M., Lima, B.H.F., Lopes, G.A.O.,  
1231 Russo, R.C., Avila, T.V., Melgaco, J.G., Oliveira, A.G., Pinto, M.A., Lima, C.X., De Paula, A.M.,  
1232 Cara, D.C., Leite, M.F., Teixeira, M.M., Menezes, G.B. (2012). Chemokines and mitochondrial  
1233 products activate neutrophils to amplify organ injury during mouse acute liver failure.  
1234 *Hepatology* 56(5), 1971—1982.

1235 Marques, P.E., Oliveira, A.G., Pereira, R.V., David, B.A., Gomides, L.F., Saraiva, A.M., Pires, D.A.,  
1236 Novaes, J.T., Patricio, D.O., Cisalpino, D., et al. (2014). Hepatic DNA deposition drives drug-  
1237 induced liver injury and inflammation in mice. *Hepatology* 61(1), 348—360.

1238 Marra, F., Tacke, F. (2014). Roles for chemokines in liver disease. *Gastroenterology* 147, 577—  
1239 594.

1240 Martin-Murphy, B.V., Holt, M.P., Ju, C. (2010). The role of damage associated molecular pattern  
1241 molecules in acetaminophen-induced liver injury in mice. *Toxicology Letters* 192, 387—394.

1242 Maruyama, R., Takemura, G., Aoyama, T., Hayakawa, K., Koda, M., Kawase, Y., Qiu, X., Ohno, Y.,  
1243 Minatoguchi, S., Miyata, K., Fujiwara, T., Fujiwara, H. (2001). Dynamic process of apoptosis in  
1244 adult rat cardiomyocytes analyzed using 48-hour videomicroscopy and electron microscopy.  
1245 *American Journal of Pathology* 159(2), 683—691.



- 1246 McDonald, B., Pittman, K., Menezes, G.B., Hirota, S.A., Slaba, I., Waterhouse, C.C.M., Beck, P.L.,  
1247 Muruve, D.A., Kubes, P. (2010). Intravascular danger signals guide neutrophils to sites of sterile  
1248 inflammation. *Science* 330(6002), 362—366.
- 1249 Melton, A., Yee, H.F. (2007). Hepatic stellate cell protrusions couple platelet-derived growth  
1250 factor-BB to chemotaxis. *Hepatology* 45(6), 1446—1453.
- 1251 Meyer, J., Lejmi, E., Fontana, P., Morel, P., Gonelle-Gispert, C., Bühler, L. (2015). A focus on the  
1252 role of platelets in liver regeneration: Do platelet-endothelial cell interactions initiate the  
1253 regenerative process? *Journal of Hepatology* 63(5), 1263—1271.
- 1254 Mihm, S. (2018). Danger-associated molecular patterns (DAMPs): Molecular triggers for sterile  
1255 inflammation in the liver. *International Journal of Molecular Sciences* 19, 3104.
- 1256 Michalopoulos, G.K. (2010). Liver regeneration after partial hepatectomy: critical analysis of  
1257 mechanistic dilemmas. *The American Journal of Pathology* 176(1), 2—13.
- 1258 Michalopoulos, G.K. (2017). Hepatostat: Liver regeneration and normal liver tissue  
1259 maintenance. *Hepatology* 65(4), 1384—1392.
- 1260 Michalopoulos, G.K., Bhushan, B. (2021). Liver regeneration: biological and pathological  
1261 mechanisms and implications. *Nature Reviews Gastroenterology & Hepatology* 18, 40—55.
- 1262 Murphy, K.E., Hall, C.L., Maini, P.K., McCue, S.W., McElwain, D.L.S. (2012). A fibrocontractive  
1263 mechanochemical model of dermal wound closure incorporating realistic growth factor  
1264 kinetics. *Bulletin of Mathematical Biology* 74, 1143—1170.
- 1265 Naik, A., Rozman, D., Belič, A. (2014). SteatoNet: The first integrated human metaolic model  
1266 with multi-layered regulation to investigate liver-associated pathologies. *PLoS Computational*  
1267 *Biology* 10(12), e1003993.
- 1268 Naito, M., Hasegawa, G., Ebe, Y., Yamamoto, T. (2004). Differentiation and function of Kupffer  
1269 cells. *Medical Electron Microscopy* 37, 16—28.
- 1270 Nakamura, K., Nonaka, H., Saito, H., Tanaka, M., Miyajima, A. (2004). Hepatocyte proliferation  
1271 and tissue remodeling is impaired after liver injury in oncostatin M receptor knockout mice.  
1272 *Hepatology* 39(3), 635—644.
- 1273 Nevzorova, Y.A., Boyer-Diaz, Z., Cubero, F.J., Gracia-Sancho, J. (2020). Animal models for liver  
1274 disease – A practical approach for translational research. *Journal of Hepatology* 73, 423—440.
- 1275 Nowatari, T., Murata, S., Fukunaga, K., Ohkohchi, N. (2014). Role of platelets in chronic liver  
1276 disease and acute liver injury. *Hepatology Research* 44, 165—172.
- 1277 O'Dell, J.R., Zetterman, R.K., Burnett, D.A. (1986). Centrilobular hepatic fibrosis following  
1278 acetaminophen-induced hepatic necrosis in an alcoholic. *JAMA* 255(19), 2636—2637.
- 1279 Olson, K.R., Davarpanah, A.H., Schaefer, E.A., Elias, N., Misdraji, J. (2017). Case 2-2017 – An 18-  
1280 year-old woman with acute liver failure. *The New England Journal of Medicine* 376: 268—278.

1281 Park, J., Holmes, W.R., Lee, S.H., Kim, H., Kim, D., Kwak, M.K., Wang, C.J., Edelstein-Keshet, L.,  
1282 Levchenko, A. (2017). Mechanochemical feedback underlies coexistence of qualitatively distinct  
1283 cell polarity patterns within diverse cell populations. *Proceedings of the National Academy of*  
1284 *Sciences* 114(28), E5750—E5759.

1285 Pinzani, M., Milani, S., Grappone, C., Weber JR., F.L., Gentilini, P., Abboud, H.E. (1994).  
1286 Expression of platelet-derived growth factor in a model of acute liver injury. *Hepatology* 19(3),  
1287 701—707.

1288 Popov, V.L. (2010). *Contact mechanics and friction*. Springer.

1289 Puche, J.E., Saiman, Y., Friedman, S.L. (2013). Hepatic stellate cells and liver fibrosis.  
1290 *Comprehensive Physiology* 3(4), 1473—1492.

1291 Ramachandran, P., Pellicoro, A., Vernon, M.A., Boulter, L., Aucott, R.L., Ali, A., Hartland, S.N.,  
1292 Snowdon, V.K., Cappon, A., Gordon-Walker, T.T., Williams, M.J., Dunbar, D.R., Manning, J.R.,  
1293 Van Rooijen, N., Fallowfield, J.A., Forbes, S.J., Iredale, J.P. (2012). Differential Ly-6C expression  
1294 identifies the recruited macrophage phenotype, which orchestrates the regression of murine  
1295 liver fibrosis. *PNAS* 109(46), E3186—E3195.

1296 Ramadori, P., Klag, T., Malek, N.P., Heikenwalder, M. (2019). Platelets in chronic liver disease,  
1297 from bench to bedside. *JHEP Reports* 1, 448—459.

1298 Ramaiah, S.K., Jaeschke, H. (2007). Role of neutrophils in the pathogenesis of acute  
1299 inflammatory liver injury. *Toxicologic Pathology* 35, 757—766.

1300 Remien, C.H., Adler, F.R., Waddoups, L., Box, T.D., Sussman, N.L. (2012). Mathematical  
1301 modeling of liver injury and dysfunction after acetaminophen overdose: Early discrimination  
1302 between survival and death. *Hepatology* 56(2), 727—734.

1303 Ritz, T., Krenkel, O., Tacke, F. (2018). Dynamic plasticity of macrophage functions in diseased  
1304 liver. *Cellular Immunology* 330, 175—182.

1305 Rohrschneider, M., Scheuermann, G., Hoehme, S., Drasdo, D. (2007). Shape characterization of  
1306 extracted and simulated tumor samples using topological and geometric measures. 29<sup>th</sup> Annual  
1307 International Conference of the IEEE Engineering in Medicine and Biology Society, 6271—6277.

1308 Rotsch, C., Braet, F., Wisse, E., Radmacher, M. (1997). AFM imaging and elasticity  
1309 measurements on living rat liver macrophages. *Cell Biology International* 21(11), 685—696.

1310 Schneider, K.M., Elfers, C., Ghallab, A., Schneider, C.V., Galvez, E.J.C., Mohs, A., Gui, W.,  
1311 Candels, L.S., Wirtz, T.H., Zuehlke, S., et al. (2021). Intestinal dysbiosis amplifies  
1312 acetaminophen-induced acute liver injury. *Cellular and Molecular Gastroenterology and*  
1313 *Hepatology* 11(4), 909—933.

1314 Schneider, K.M., Candels, L.S., Hov, J.R., Myllys, M., Hassan, R., Schneider, C.V., et al. (2021).  
1315 Gut microbiota depletion exacerbates cholestatic liver injury via loss of FXR signaling. *Nat.*  
1316 *Metab.* 3, 1228—1241.

1317 Schuran, F.A., Lommetz, C., Steudter, A., Ghallab, A., Wieschendorf, B., Schwinge, D., Zuehlke,  
 1318 S., Reinders, J., Heeren, J., Lohse, A.W., et al. (2021). Aryl hydrocarbon receptor activity in  
 1319 hepatocytes sensitizes to hyperacute acetaminophen-induced hepatotoxicity in mice. *Cellular*  
 1320 *and Molecular Gastroenterology and Hepatology* 11(2), 371—388. Seki, E., De Minicis, S.,  
 1321 Österreicher, C.H., Kluwe, J., Osawa, Y., Brenner, D.A., Schwabe, R.F. (2007) TLR4 enhances TGF-  
 1322  $\beta$  signaling and hepatic fibrosis. *Nature Medicine* 13(11), 1324—1332.

1323 Schwarz, U.S. (2020). To buckle or not to buckle. *Nature Materials* 19, 8—9.

1324 Schwen, L.O., Krauss, M., Niederalt, C., Gremse, F., Kiessling, F., Schenk, A., Preusser, T. (2014).  
 1325 Spatio-temporal simulation of first pass drug perfusion in the liver. *PLoS Computational Biology*  
 1326 10(3), e1003499.

1327 Schwen, L.O., Kuefer, L., Preusser, T. (2016). Modeling approaches for hepatic spatial  
 1328 heterogeneity in pharmacokinetic simulations. *Drug Discovery Today Disease Models* 22, 35—  
 1329 43.

1330 Seki, E., De Minicis, S., Österreicher, C.H., Kluwe, J., Osawa, Y., Brenner, D.A., Schwabe, R.F.  
 1331 (2007). TLR4 enhances TGF- $\beta$  signaling and hepatic fibrosis. *Nature Medicine* 13, 1324—1332.

1332 Sezgin, S., Hassan, R., Zuehlke, S., Kuepfer, L., Hengstler, J.G., Spiteller, M., Ghallab, A. (2018).  
 1333 Spatio-temporal visualization of the distribution of acetaminophen as well as its metabolites  
 1334 and adducts in mouse livers by MALDI MSI. *Archives of Toxicology* 92(9), 2963—2977.

1335 Sieber, P., Schaefer, A., Lieberherr, R., Goff, F.L., Stritt, M., Welford, R.W.D., Gatfield, J., Peter,  
 1336 O., Nayler, O., Luethi, U. (2018). Novel high-throughput myofibroblast assays identify agonists  
 1337 with therapeutic potential in pulmonary fibrosis that act via EP<sub>2</sub> and EP<sub>4</sub> receptors. *PLOS ONE*  
 1338 13(11), e0207872.

1339 Soyombo, A.A., DiCorleto, P.E. (1994). Stable expression of human platelet-derived growth  
 1340 factor B chain by bovine aortic endothelial cells. *The Journal of Biological Chemistry* 269(26),  
 1341 17734—17740.

1342 Stepanova, D., Byrne, H.M., Maini, P.K., Alarcon, T. (2021). A multiscale model of complex  
 1343 endothelial cell dynamics in early angiogenesis. *PLoS Computational Biology* 17(1), e1008055.

1344 Stewart, R.K., Dangi, A., Huang, C., Murase, N., Kimura, S., Stolz, D.B., Wilson, G.C., Lentsch,  
 1345 A.B., Gandhi, C.R. (2014). A novel mouse model of depletion of stellate cells clarifies their role  
 1346 in ischemia/reperfusion- and endotoxin-induced acute liver injury. *Journal of Hepatology* 60,  
 1347 298—305.

1348 Shi, C., Jia, T., Mendez-Ferrer, S., Hohl, T.M., Serbina, N.V., Lipuma, L., Leiner, I., Li, M.O.,  
 1349 Frenette, P.S., Pamer, E.G. (2011). Bone marrow mesenchymal stem and progenitor cells induce  
 1350 monocyte emigration in response to circulating Toll-like receptor ligands. *Immunity* 34(4),  
 1351 590—601.

1352 Stravitz, R.T., Ellerbe, C., Durkalski, V., Reuben, A., Lisman, T., Lee, M.W., the Acute Liver Failure  
 1353 Study Group. (2017). Thrombocytopenia is associated with multi-organ system failure in  
 1354 patients with acute liver failure. *Clinical Gastroenterology & Hepatology* 14(4), 613—620.

1355 Sun, D., Novotny, M., Bulek, K., Liu, C., Li, X., Hamilton, T. (2011). Treatment with IL-17 prolongs  
 1356 the half-life of chemokine CXCL1 mRNA via the adaptor TRAF5 and the splicing-regulatory factor  
 1357 SF2 (ASF). *Nature Immunology* 12(9), 853—860.

1358 Tacke, F., Zimmermann, H.W. (2014). Macrophage heterogeneity in liver injury fibrosis. *Journal*  
 1359 *of Hepatology* 60, 1090—1096.

1360 Talman, L., Agmon, E., Peirce, S.M., Covert, M.W. (2019). Multiscale models of infection.  
 1361 *Current Opinion in Biomedical Engineering* 11, 102—108.

1362 Tangkijvanich, P., Tam, S.P., Yee, J.F. (2001). Wound-induced migration of rat hepatic stellate  
 1363 cells is modulated by endothelin-1 through Rho-kinase-mediated alterations in the acto-myosin  
 1364 cytoskeleton. *Hepatology* 3(1), 74—80.

1365 Thurley, K., Gerecht, D., Friedmann, E., Hoefer, T. (2015). Three-dimensional gradients of  
 1366 cytokine signaling between T cells. *PLoS Computational Biology* 11(4), e1004206.

1367 Trepap, X., Wasserman, M.R., Angelini, T.E., Millet, E., Weitz, D.A., Butler, J.P., Fredberg, J.J.  
 1368 (2009). Physical forces during collective cell migration. *Nature Physics* 5(6), 426—430.

1369 Troeger, J.S., Mederacke, I., Gwak, G., Dapito, D.H., Mu, X., Hsu, C.C., Pradere, J., Friedman,  
 1370 R.A., Schwabe, R.F. (2012). Deactivation of hepatic stellate cells during liver fibrosis resolution  
 1371 in mice. *Gastroenterology* 143(4), 1073—1083.

1372 Van Coillie, E., Van Damme, J., Opdenakker, G. (1999). The MCP/eotaxin subfamily of CC  
 1373 chemokines. *Cytokine & Growth Factor Reviews* 10(1), 61—86.

1374 Van Liedekerke, P., Palm, M.M., Jagiella, N., Drasdo, D. (2015). Simulating tissue mechanics with  
 1375 agent-based models: concepts, perspectives, and some novel results. *Computational Particle*  
 1376 *Mechanics* 2(4): 401—444.

1377 Van Liedekerke, P., Neitsch, J., Johann, T., Alessandri, K., Nassoy, P., Drasdo, D. (2019).  
 1378 Quantitative agent-based modeling reveals mechanical stress response of growing tumor  
 1379 spheroids is predictable over various growth conditions and cell lines. *PLoS Computational*  
 1380 *Biology* 15(3), e1006273.

1381 Van Liedekerke, P., Neitsch, J., Johann, T., Warnt, E., Gonzalez-Valverde, I., Hoehme, S.,  
 1382 Grosser, S., Kaes, J., Drasdo, D. (2020). A quantitative high-resolution computational mechanics  
 1383 cell model for growing and regenerating tissues. *Biomechanics and Modeling in*  
 1384 *Mechanobiology* 19(1), 189—220.

1385 Verma, B.K., Subramaniam, P., Vadigepalli, R. (2019). Model-based virtual patient analysis of  
 1386 human liver regeneration predicts critical perioperative factors controlling the dynamic mode of  
 1387 response to resection. *BMC Systems Biology* 13(1), 1—15.

1388 Vishwakarma, M., Di Russo, J., Probst, D., Schwarz, U.S., Das, T., Spatz, J.P. (2018). Mechanical  
1389 interactions among followers determine the emergence of leaders in migrating epithelial cell  
1390 collectives. *Nature Communications* 9(1), 1–12.

1391 Waltenberger, J., Usuki, K., Fellström, B., Funa, K., Heldin, C. (1992). Platelet-derived endothelial  
1392 cell growth factor Pharmacokinetics, organ distribution and degradation after intravenous  
1393 administration in rats. *FEBS Letters* 313(2), 129–132.

1394 Wake, K. (2006). Hepatic stellate cells: Three-dimensional structure, localization, heterogeneity  
1395 and development. *Proceedings of the Japan Academy, Series B* 82(4), 155–164.

1396 Wakefield, L.M., Winokur, T.S., Hollands, R.S., Christopherson, K., Levinson, A.D., Sporn, M.B.  
1397 (1990). Recombinant latent transforming growth factor  $\beta$ 1 has a longer plasma half-life in rats  
1398 than active transforming growth factor  $\beta$ 1, and a different tissue distribution. *The Journal of*  
1399 *Clinical Investigation* 86(6), 1976–1984.

1400 Wambaugh, J., Shah, I. (2010). Simulating microdosimetry in a virtual hepatic lobule. *PLoS*  
1401 *Computational Biology* 6(4), e1000756.

1402 Willemsen, L., de Winther, M.P.J. (2020). Macrophage subsets in atherosclerosis as defined by  
1403 single-cell technologies. *Journal of Pathology* 250, 705–714.

1404 Yang, C., Zeisberg, M., Mosterman, B., Sudhakar, A., Yerramalla, U., Holthaus, K., Xu, L., Eng, F.,  
1405 Afdhal, N., Kalluri, R. (2003). Liver fibrosis: insights into migration of hepatic stellate cells in  
1406 response to extracellular matrix and growth factors. *Gastroenterology* 124(1), 147–159.

1407 Yang, Y., Liao, J., Lin, C., Chang, C., Wang, S., Ju, M. (2012). Characterization of cholesterol-  
1408 depleted or -restored cell membranes by depth-sensing nano-indentation. *Soft Matter* 8(3),  
1409 682–687.

1410 You, Q., Holt, M., Yin, H., Li, G., Hu, C., Ju, C. (2013). Role of hepatic resident and infiltrating  
1411 macrophages in liver repair after acute injury. *Biochemical Pharmacology* 86(6), 836–843.

1412 Zandarashvili, L., Sahu, D., Lee, K., Lee, Y.S., Singh, P., Rajarathnam, K., Iwahara, J. (2013). Real-  
1413 time kinetics of high-mobility group box 1 (HMGB1) oxidation in extracellular fluids studied by  
1414 in Situ protein NMR spectroscopy. *Journal of Biological Chemistry* 288(17), 11621–11627.

1415 Zieve, L., Anderson, W.R., Dozeman, R., Draves, K., Lyftogt, C. (1985). Acetaminophen liver  
1416 injury: sequential changes in two biochemical indices of regeneration and their relationship to  
1417 histologic alterations. *The Journal of Laboratory and Clinical Medicine* 105(5), 619–624.

1418 Zigmond, E., Samia-Grinberg, S., Pasmanik-Chor, M., Brazowski, E., Shibolet, O., Halpern, Z.,  
1419 Varol, C. (2014). Infiltrating monocyte-derived macrophages and resident Kupffer cells display  
1420 different ontogeny and functions in acute liver injury. *Journal of Immunology* 193, 344–353.

## 1421 **ACKNOWLEDGEMENTS**

1422 The authors acknowledge financial support from BMBF LiSyM FKZ: 031L0045, BMBF  
1423 LiSyM-Krebs: 031L0257D, ANR iLite, ANR-16-RHUS-0005. A.G. was funded by the German-  
1424 Research-Foundation (DFG; GH 276). S.D. was funded by LiSyM Grant PTJ-FKZ: 031L0043.

## 1425 **AUTHOR CONTRIBUTIONS**

1426 The modeling part was performed by D.D. and J.Z., the experimental part by A.G., R.H., J.G.H.

1427 **Conceptualization:** D.D.; **Data curation:** J.Z., A.G., R.H.; **Formal analysis:** J.Z., A.G., D.D., **Funding**  
1428 **acquisition:** A.G., S.D., J.G.H., D.D.; **Investigation:** D.D., J.Z.; **Methodology:** D.D., J.Z. (modeling);  
1429 A.G., J.G.H. (experimental); **Project administration:** D.D.; **Resources:** D.D., J.G.H.; **Software**  
1430 **implementation:** J.Z.; **Supervision:** D.D., A.G.; **Validation:** D.D., J.Z., A.G., S.D., J.G.H.;  
1431 **Visualization:** J.Z.; **Writing, Original Draft:** J.Z. and D.D.; **Writing, Review and Editing:** J.Z., A.G.,  
1432 S.D., J.G.H., D.D.

## 1433 **DECLARATION OF INTERESTS**

1434 The authors declare no competing interests.

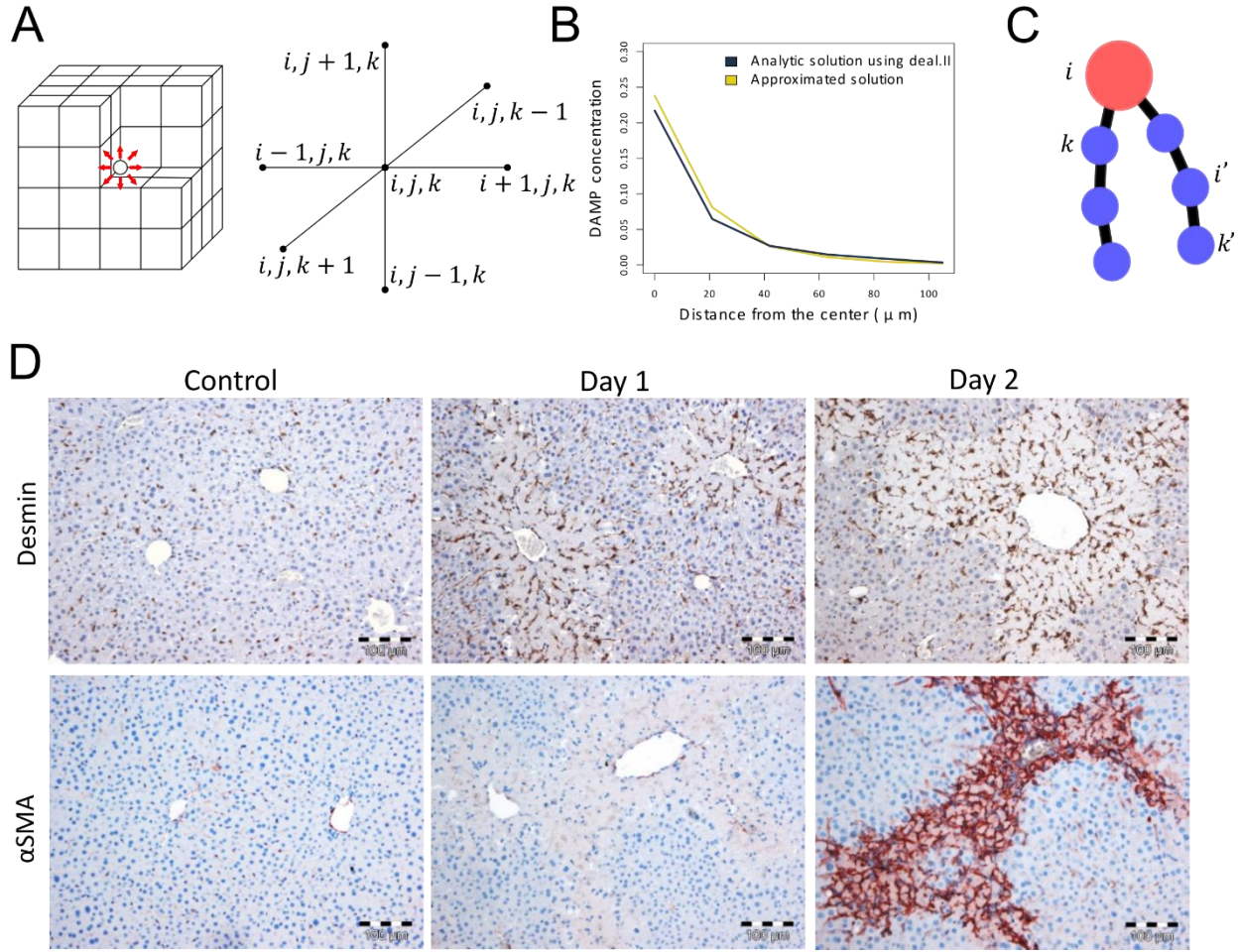


**Figure S1. The cubic system to simulate the signal gradient and the staining of HSCs before day 2.** (A) A cubic system is used to approximate the solution of PDE regarding a signal gradient in the lobule. (B) Comparison of the approximated solution of the concentration of a DAMP released by one hepatocyte with the corresponding analytic solution by using software deal.II (Arndt et al., 2021). (C) HSC number  $i$  is modeled as one head sphere (red) connected with several arms (in the simulation, 5 arms are used while in C only 2 arms are represented for simplicity) represented as chains of spheres (blue). There are elastic forces between every sphere and its connected neighboring spheres. Then elastic force on  $i'$  from  $k'$  is defined as  $\vec{F}_{ela,i'k'} = \vec{e}_{i'k'} \Delta L_{i'k'} E_{HSC} \pi R_{HSC,arm}^2 / L_{i'k'}$ , where  $E_{HSC}$  is the Young's modulus of HSC,  $R_{HSC,arm}$  is the radius of the arm spheres (we assume it is 1/3 of the radius of head sphere of HSC),  $L_{i'k'}$  is the equilibrium length of  $i'k'$ ,  $\Delta L_{i'k'}$  is the deviation from  $L_{i'k'}$ ,  $\vec{e}_{i'k'}$  is unit vector from  $i'$  to  $k'$ . In the interaction with other cell types, only the head sphere of  $i$  (red) is considered. (D) The staining of all types of HSCs (Desmin) and activated HSCs ( $\alpha$ SMA).

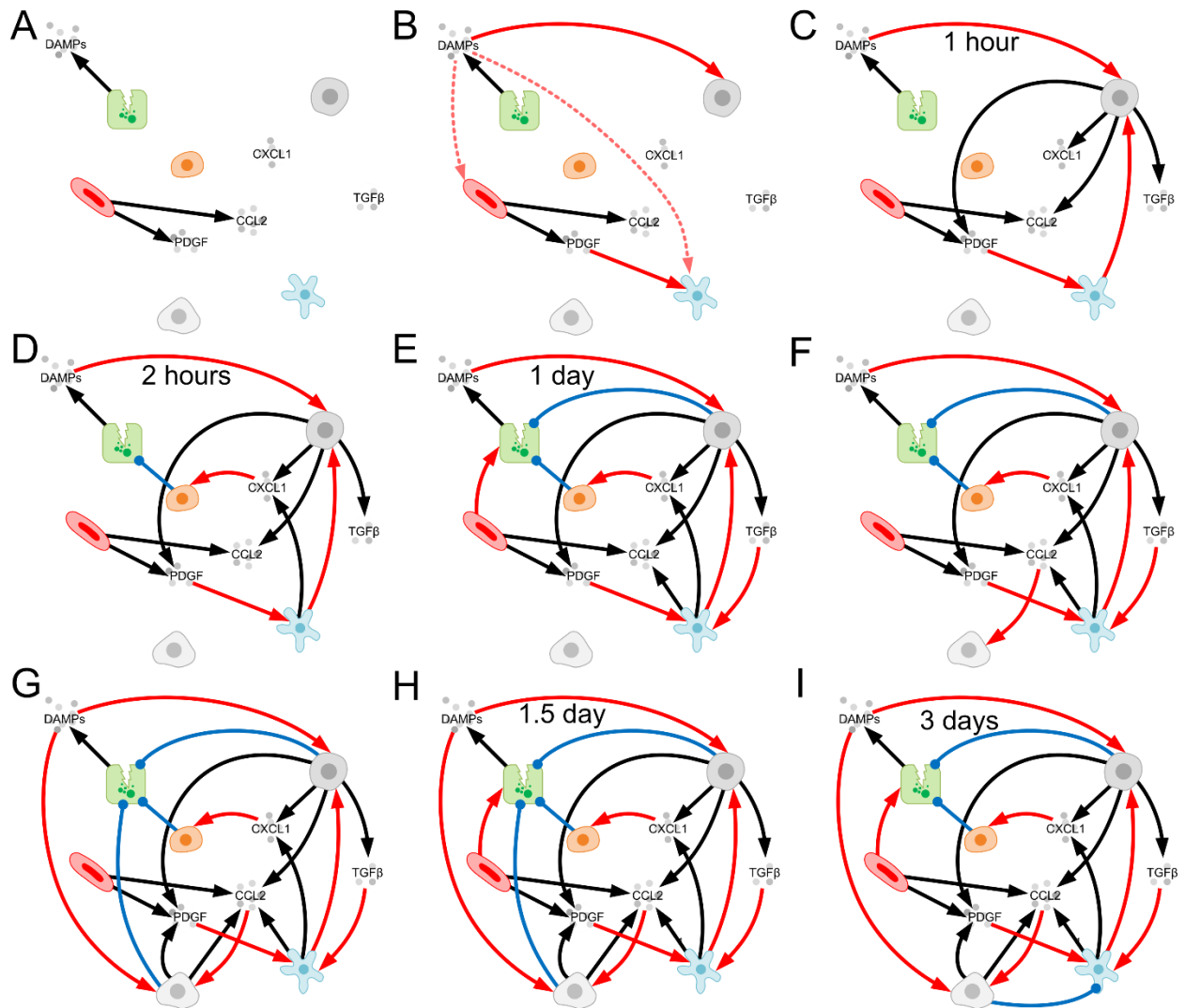
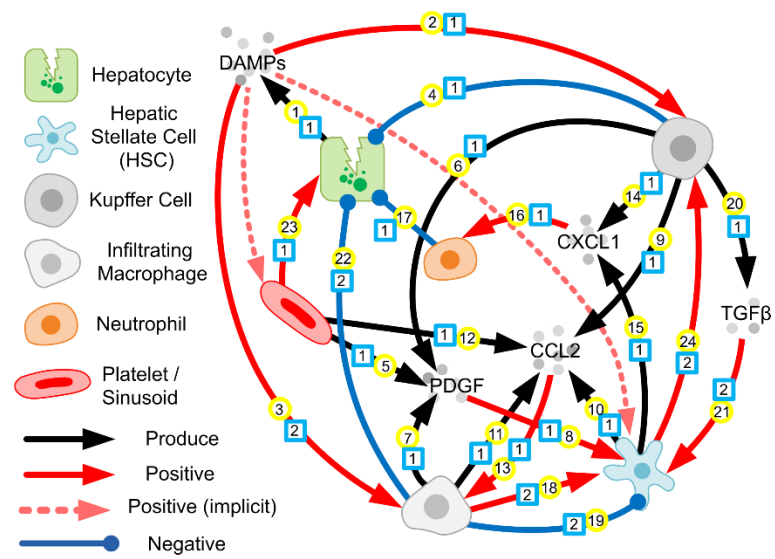




**Figure S2. Time course of the interaction processes in the reference state.** (A-C) About 1 hour after drug administration: Injured hepatocytes secrete DAMPs to activate Kupffer cells, which secrete CXCL1, CCL2 and TGF $\beta$ . Platelets secrete PDGF and CCL2. HSCs are attracted by PDGF. From activation on, the Kupffer cell population decreases until day 2 due to the cell death, before it recovers again. (D) About 2 hours after APAP administration, neutrophils are attracted by CXCL1 to induce the death of injured hepatocytes. Kupffer cells migrate towards HSCs. (E-G) Around 1 day after APAP administration, HSCs are activated by TGF $\beta$  and secrete CCL2 and CXCL1. Infiltrating macrophages are attracted by CCL2 and activated by DAMPs. Both, infiltrating macrophages and Kupffer cells phagocytose dead hepatocytes. (H) Around 1.5 days after APAP administration, healthy hepatocytes surrounding the necrotic region proliferate and migrate to recover the lesion. (I) Around 3 days after APAP administration, infiltrating macrophages switched from Ly6C-high to Ly6C-low phenotype and revert/remove activated HSCs.

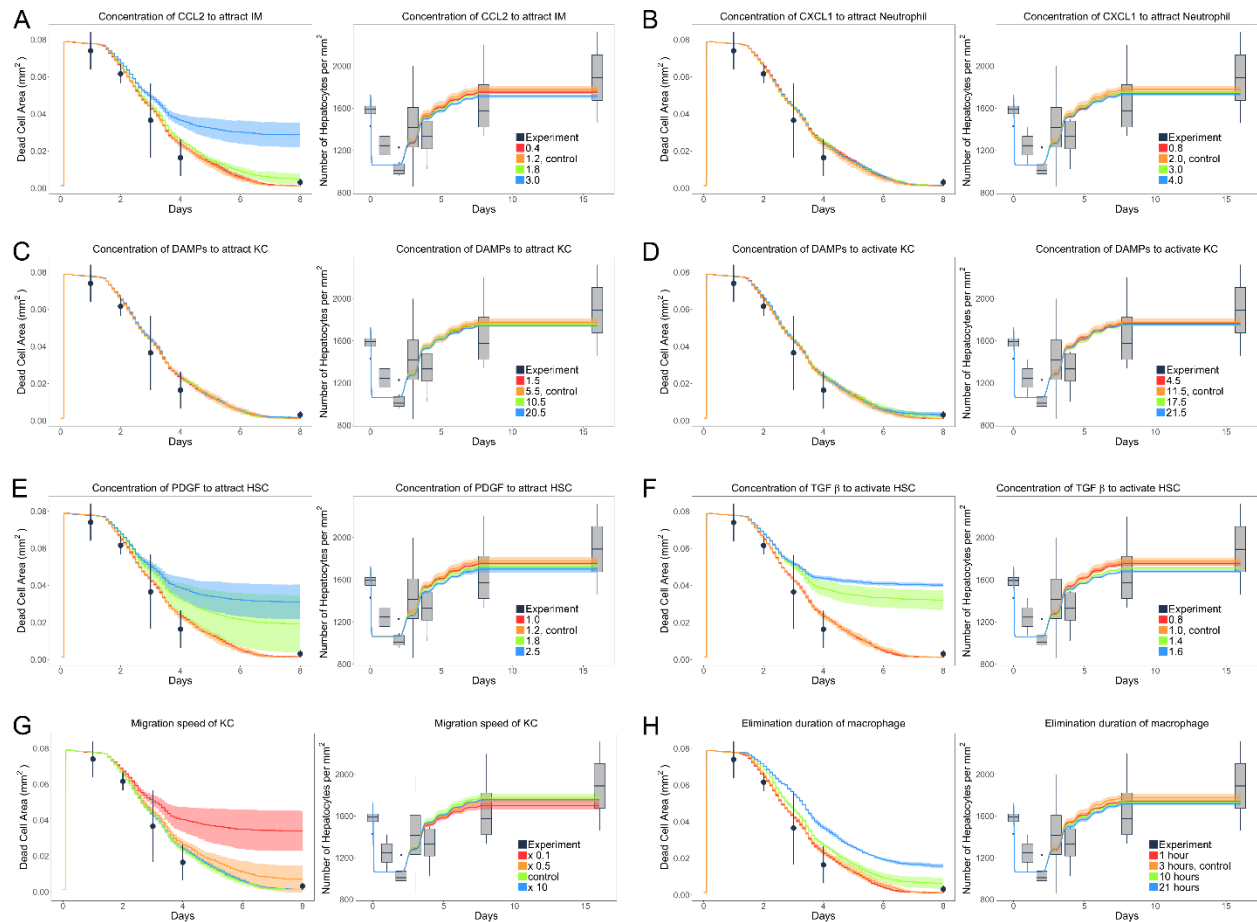


**Figure S3. Sensitivity test of the impact of signal concentrations on liver regeneration.** Concentration of different signals: (A) CCL2: attract the infiltration of macrophages. (B) CXCL1: attract neutrophils. (C) DAMP: attracts Kupffer cells. (D) DAMP: activates Kupffer cells. (E) PDGF: attracts HSCs. (F) TGF $\beta$ : activates HSCs. (G) Migration speed of Kupffer cells. (H) Elimination duration of macrophages.

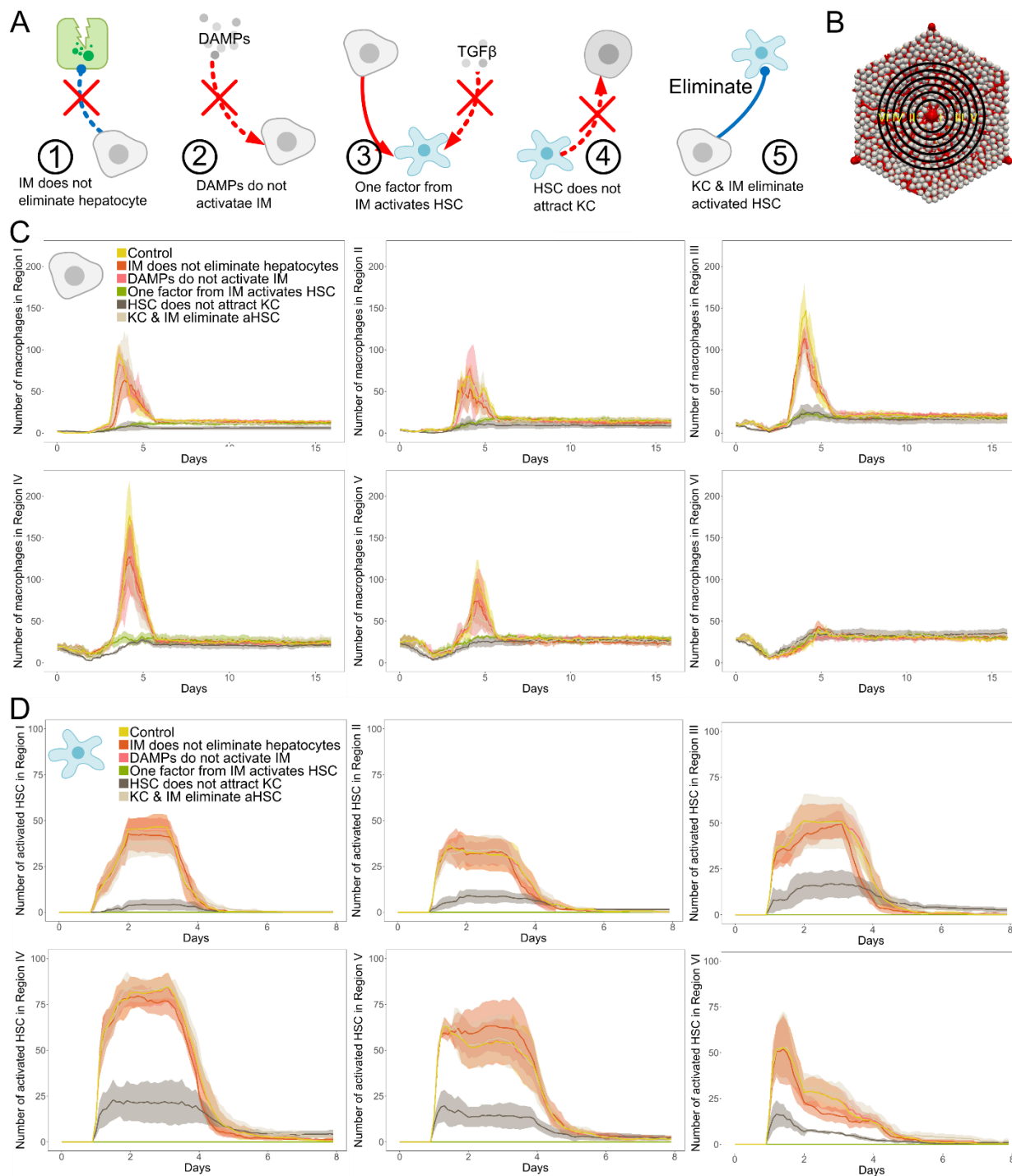


**Figure S4. Number of macrophages and activated HSCs during liver regeneration under different perturbed interactions.** (A) Illustration of five perturbed interactions. “IMs eliminate hepatocytes: no” corresponds to the perturbation that infiltrating macrophages cannot eliminate dead hepatocytes; “DAMPs activate IMs: no” corresponds to the perturbation that DAMPs cannot activate infiltrating macrophages; “TGF $\beta$  activates HSCs: no” corresponds to the perturbation that a factor produced by infiltrating macrophages rather than TGF $\beta$  activates HSCs; “KCs migrate to HSCs: no” corresponds to the perturbation that Kupffer cells cannot

migrate towards HSCs; “IMs eliminate aHSCs” corresponds to the perturbation that infiltrating macrophages eliminate the activated HSCs rather than switch them back to the quiescent phenotype. (B) Spatial distribution of activated HSCs and macrophages in the lobule, measured by counting the corresponding number in six regions according to its distance to the central vein. (C and D) Number of macrophages and activated HSCs in each region over time under five perturbed interactions. Absolute numbers are estimated from the corresponding cell densities taken from literature (Wake, 2006 & Bouwens et al., 1986), which might not match with the real cell number in the lobule.

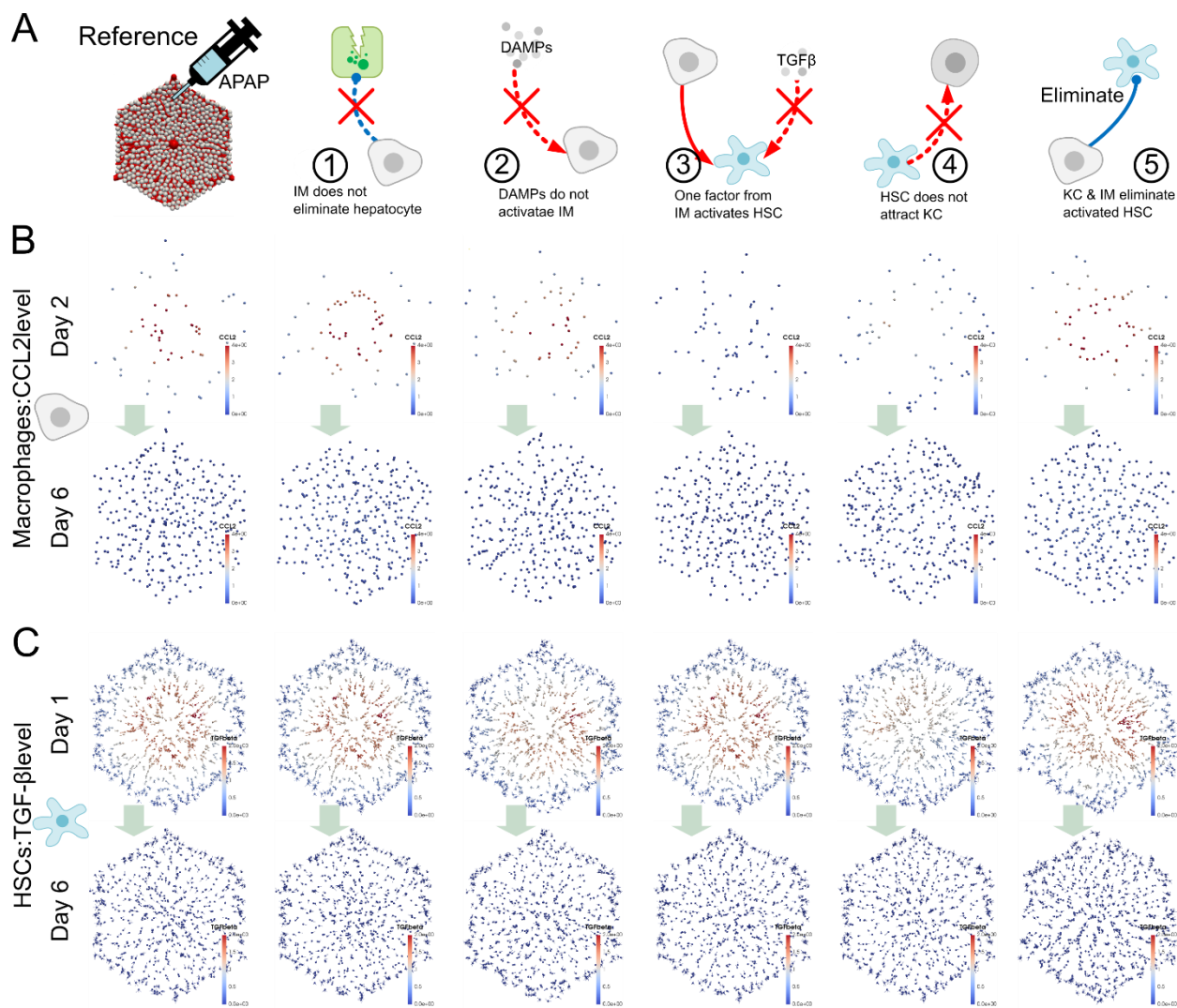


**Figure S5. Molecular expression levels of signaling molecules in the reference state and five perturbed cases.** (A) Illustration of five perturbed interactions. (B) The local level of CCL2 at macrophages. (C) The local level of TGFβ at HSCs.

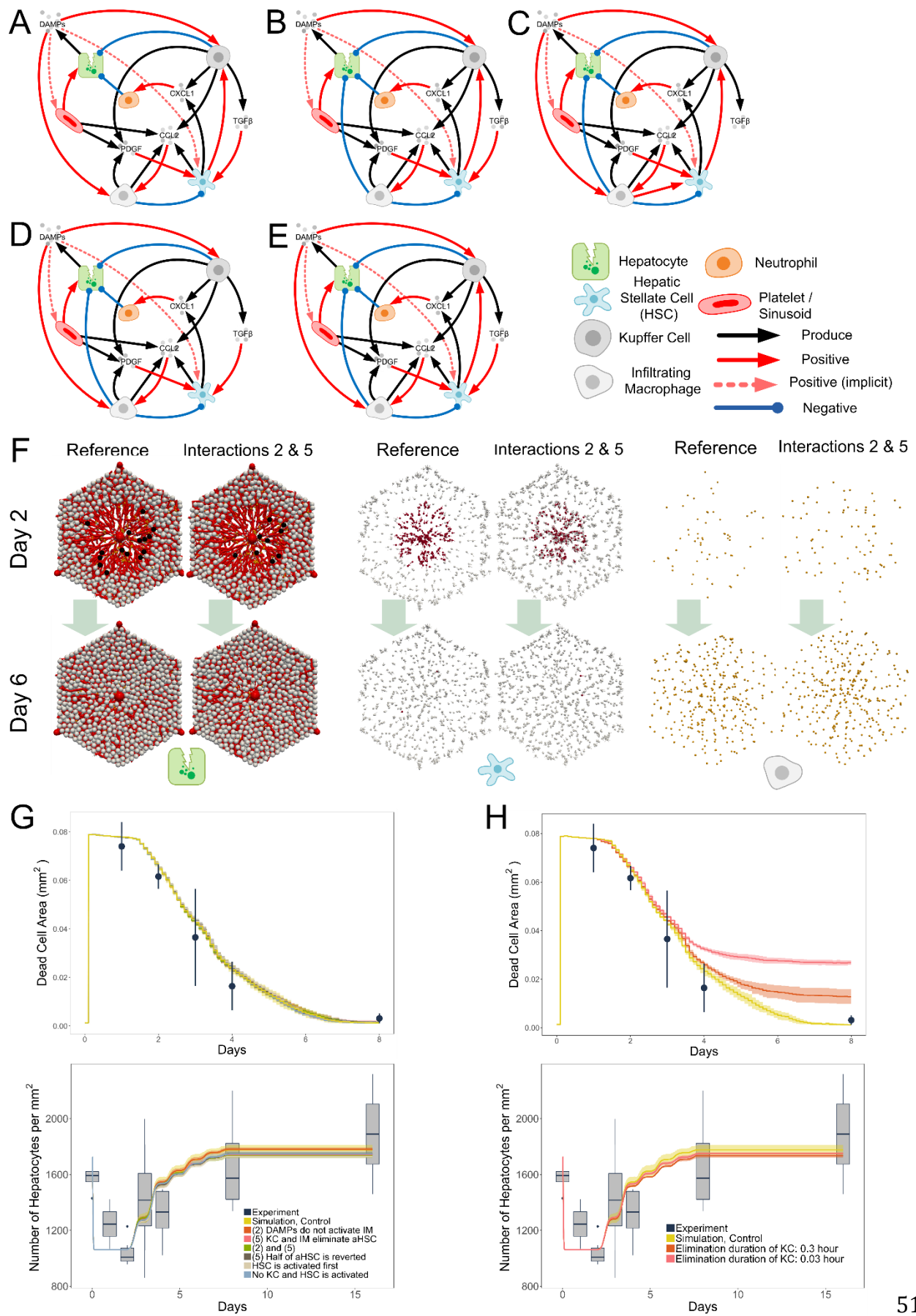


**Figure S6. Network integrating possible and interpreted interactions.** Network where (A) infiltrating macrophages do not eliminate the dead hepatocytes; (B) DAMPs do not activate the infiltrating macrophages; (C) one factor released by infiltrating macrophages (not TGF $\beta$ ) activates the HSCs; (D) KCs do not migrate towards the HSCs; (E) infiltrating macrophages eliminate the activated HSCs, are presented. (F) Simulations using the network that integrates the two interactions that “DAMPs do not activate the infiltrating macrophages” and “infiltrating macrophages eliminate the activated HSCs”. Snapshots of the different cell types at days 2 & 6 are shown. (G) The corresponding curves of lesion area and hepatocytes density are displayed. (H) For the interaction “infiltrating macrophages do not eliminate the dead hepatocytes”, different phagocytosis capacities of the Kupffer cells (elimination duration time) are tested: lesion area and hepatocytes density are displayed.



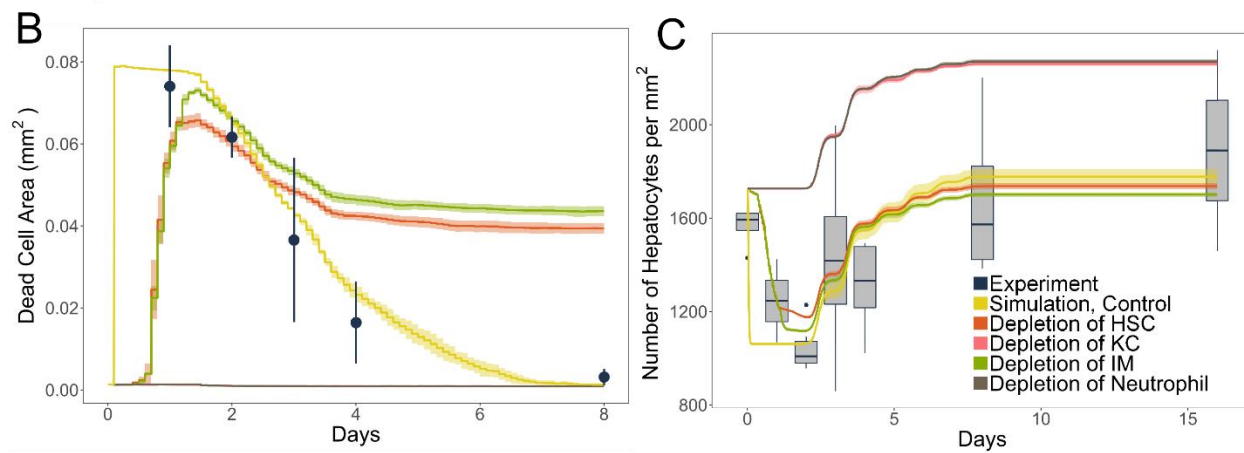
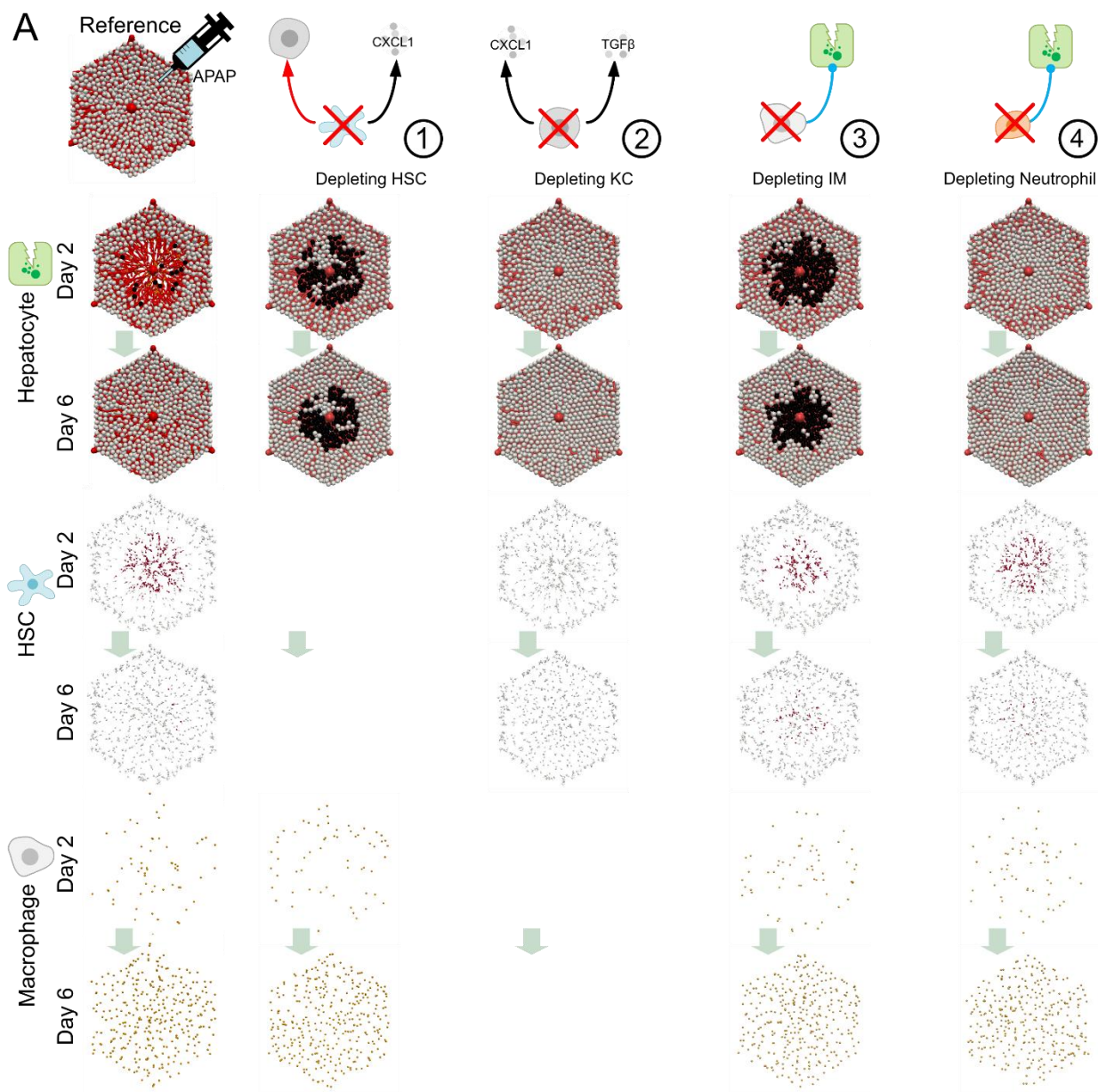


**Figure S7. Pattern of regeneration in the liver lobule after abrogating NAPQI and depleting different cell types of.** Here, a hypothetical case of regeneration from a necrotic lesion is considered that has been alternatively generated by cell-death triggered independent of the NAPQI-pathway. (A) The regenerating lobule over time of the reference state and upon individual depletion of four sinusoidal cell types: (1) Depletion of HSCs; (2) depletion of Kupffer cells; (3) depletion of infiltrating macrophages; (4) depletion of neutrophils. For hepatocytes, white represents the healthy ones, black represents the dead ones. For HSCs, white represents the quiescent ones, red represents the activated ones. (B and C) Lesion area and hepatocytes density over time in the reference state and upon individual depletion of different cell types. Upon depletion of HSCs, due to the decreased CXCL1 levels, the number of neutrophils infiltrating into the lesion is reduced, leading to generally reduced numbers of neutrophils, Kupffer cells, and infiltrating macrophages in the lesion. As consequence, a large number of dead hepatocytes remains uncleared in the lobule. Depletion of Kupffer cells leads to a non-necrotic lesion in the lobule. Due to the lack of Kupffer cells, therefore reduced TGF $\beta$  signal to trigger the activation of HSCs regarding the secretion of CXCL1, consequently, lower levels of CXCL1 production, reduced neutrophil attraction and diminished hepatocyte injury. The depletion of infiltrating macrophages does almost not affect the size of the necrotic lesion, but only reduces its clearance from dead hepatocytes. After the depletion of neutrophils (Fig. S7A, scenario 4), since neutrophils are responsible to kill injured hepatocytes, all injured hepatocytes in the lesion remain non-necrotic if neutrophils are depleted. Therefore, the lesion area remains to be zero.

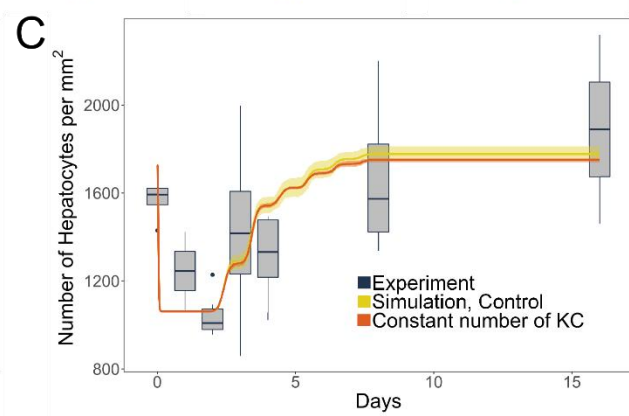
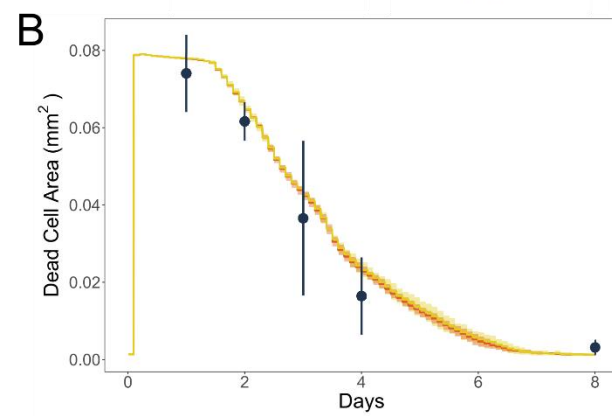
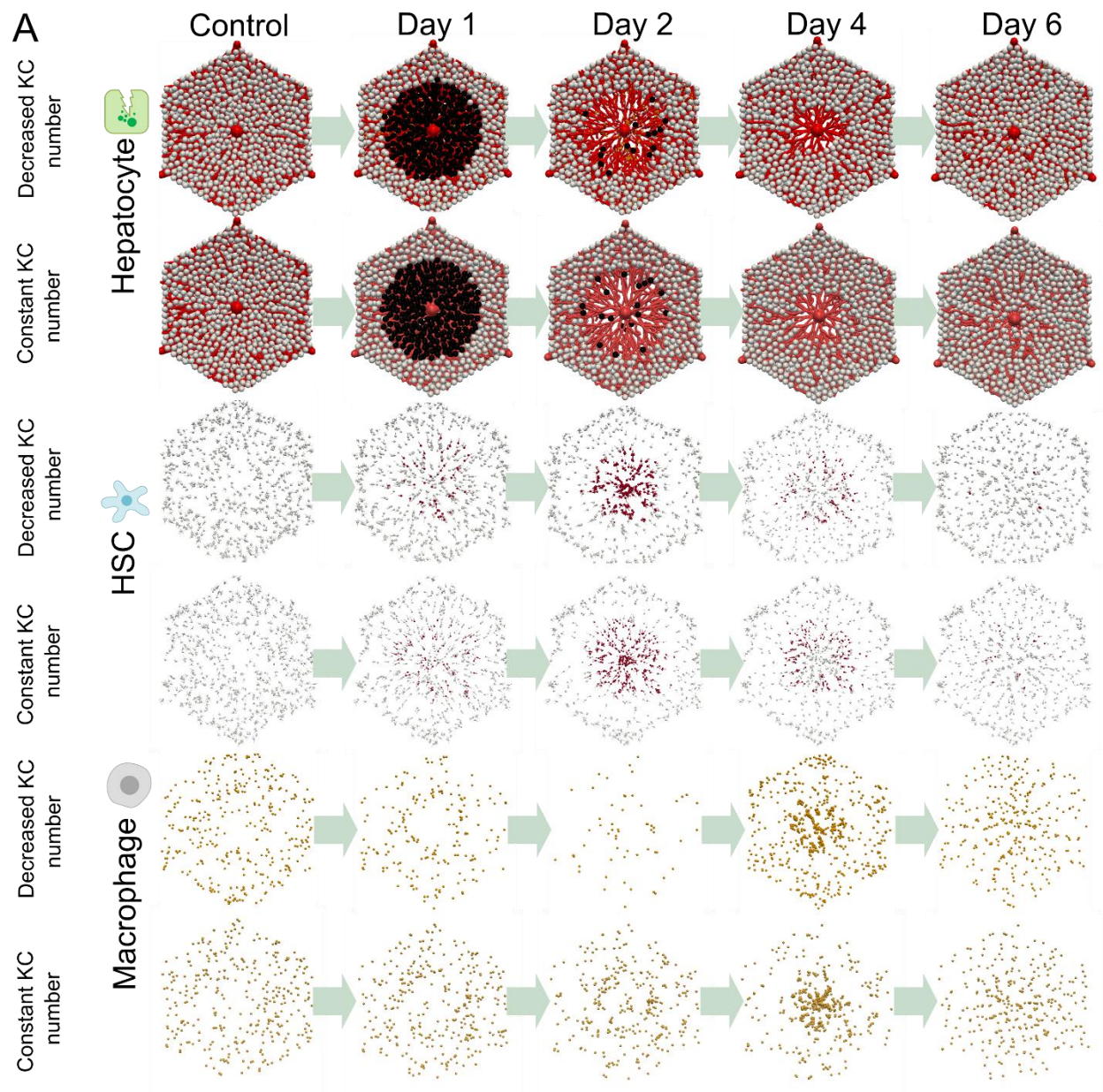




**Figure S8.** Pattern of liver regeneration with constant numbers of Kupffer cells. (A) The regenerating lobule over time in the reference state and with assuming a constant number of Kupffer cells. (B) Dead cells area over time. (C) Hepatocytes density over time.

**Table S1.** List of parameters used in the study, related to Figure 1.

Parameter	Description	Value	Reference
$r_{Hep}$	Hepatocyte radius	$\sim 10.7 \mu\text{m}$	Estimated from data
$r_{sin}$	Sinusoid radius	$\sim 2.1 \mu\text{m}$	Estimated from data
$r_{HSC}$	HSC nucleus radius (head sphere of HSC)	$\sim 2 \mu\text{m}$	Wake, 2006
$l_{HSC,branch}$	HSC branch length	$\sim 12 \mu\text{m}$	Wake, 2006
$r_{KC}$	Kupffer cell radius	$\sim 4 \mu\text{m}$	Gardin et al., 1992
$r_{IM}$	Infiltrating macrophage radius	$\sim 6 \mu\text{m}$	Shi et al., 2011
$r_{Neutrophil}$	Neutrophil radius	$\sim 4 \mu\text{m}$	Herant et al., 2005
$K_{Hep}$	Young's modulus of hepatocyte	$\sim 450 \text{ Pa}$	Hoehme et al., 2010
$K_{sin}$	Young's modulus of sinusoid	$\sim 600 \text{ Pa}$	Hoehme et al., 2010
$K_{HSC}$	Young's modulus of HSC	$\sim 700 \text{ Pa}$	Estimated from fibroblast, Yang et al., 2012
$K_{KC}$	Young's modulus of Kupffer cell	$\sim 3100 \text{ Pa}$	Rotsch et al., 1997
$K_{IM}$	Young's modulus of infiltrating macrophage	$\sim 1400 \text{ Pa}$	Estimated from immune macrophage, Bui et al., 2015
$K_{Neutrophil}$	Young's modulus of neutrophil	$\sim 1500 \text{ Pa}$	Lee et al., 2011
$\nu$	Poisson ratio of all cell types	0.4	Hoehme et al., 2010
NA	Cell cycle time of hepatocyte	24 hours	Hoehme et al., 2010
$\Gamma_{ECM,cell}$	Cell-medium friction (all cell types except HSC)	$10^8 \text{ Ns/m}^3$	Estimated
$\Gamma_{ECM,HSC}$	HSC-medium friction	$10^{10} \text{ Ns/m}^3$	Estimated

$\Gamma_{\parallel,SE}, \Gamma_{\parallel,SS}, \gamma_{\perp}, \gamma_{\parallel}$	Friction between all cell types including sinusoids	$10^8 \text{ Ns/m}^3$	Estimated
$Den_{HSC}$	HSC density in the liver	$\sim 1/70 \mu\text{m}$ of the sinusoid	Wake, 2006
$Den_{KC}$	Kupffer cell density in the liver	$\sim 2 \times 10^4 / \text{mm}^3$	Bouwens et al., 1986
$Den_{IM}$	Infiltrating macrophage density in the liver	$\sim 2 \times Den_{KC}$	Estimated from Zigmond et al., 2014
$Den_{Neutrophil}$	Neutrophil density in the liver	$\sim 1.9 \times 10^{-3} / \mu\text{m}^2$ of the lesion	McDonald et al., 2010
$sp_{HSC,mean}$	Mean of migration speed of HSC	$\sim 2.1 \mu\text{m}/\text{hour}$	Tangkijvanich et al., 2001
$sp_{HSC,SD}$	SD of migration speed of HSC	$\sim 0.1 \mu\text{m}/\text{hour}$	Tangkijvanich et al., 2001
$sp_{KC,mean}$	Mean of migration speed of Kupffer cell	$\sim 0.04 \mu\text{m}/\text{min}$	Based on Ju and Tacke, 2016
$sp_{KC,SD}$	SD of migration speed of Kupffer cell	$\sim 0.01 \mu\text{m}/\text{min}$	Based on Ju and Tacke, 2016
$sp_{IM,mean}$	Mean of migration speed of infiltrating macrophage	$\sim 5 \mu\text{m}/\text{min}$	Grabher et al., 2007
$sp_{IM,SD}$	SD of migration speed of infiltrating macrophage	$\sim 1.8 \mu\text{m}/\text{min}$	Grabher et al., 2007
$sp_{Neutrophil,mean}$	Mean of migration speed of neutrophil	$\sim 0.12 \mu\text{m}/\text{second}$	McDonald et al., 2010
$sp_{Neutrophil,SD}$	SD of migration speed of neutrophil	$\sim 0.02 \mu\text{m}/\text{second}$	McDonald et al., 2010
$D_{TGF\beta}$	Diffusion rate of TGF $\beta$ , estimated from its molecular weight, 25 kDa	$2.6 \times 10^{-11} \text{ m}^2/\text{s}$	Murphy et al., 2012
$D_{DAMP}$	Diffusion rate of DAMP, estimated from its molecular weight, 28 kDa	$2.5 \times 10^{-11} \text{ m}^2/\text{s}$	Davies et al., 2018
$D_{CCL2}$	Diffusion rate of CCL2, estimated from its molecular weight, 13 kDa	$3.3 \times 10^{-11} \text{ m}^2/\text{s}$	Van Coillie et al., 1999
$D_{PDGF}$	Diffusion rate of PDGF, estimated from its molecular weight, 30 kDa	$2.4 \times 10^{-11} \text{ m}^2/\text{s}$	Soyombo and DiCorleto, 1994
$D_{CXCL1}$	Diffusion rate of CXCL1, estimated from its molecular weight, 21 kDa	$2.8 \times 10^{-11} \text{ m}^2/\text{s}$	Amiri and Richmond, 2003

$\gamma_{TGF\beta}$	Decay rate of TGF $\beta$ , estimated from its half-life, 120 s	$5.8 \times 10^{-3}$ /s	Wakefield et al., 1990
$\gamma_{DAMP}$	Decay rate of DAMP, estimated from its half-life, 1000 s	$5.7 \times 10^{-4}$ /s	Zandarashvili et al., 2013
$\gamma_{CCL2}$	Decay rate of CCL2, estimated from its half-life, 1200 s	$5.8 \times 10^{-4}$ /s	Berchiche et al., 2011
$\gamma_{PDGF}$	Decay rate of PDGF, estimated from its half-life, 600 s	$1.1 \times 10^{-3}$ /s	Waltenberger et al., 1992
$\gamma_{CXCL1}$	Decay rate of CXCL1, estimated from its half-life, 900 s	$7.7 \times 10^{-4}$ /s	Sun et al., 2011
$\phi_{DAMP,migrate}$	Concentration of DAMP to trigger Kupffer cell to migrate	5.5	Estimated
$\phi_{DAMP,activate}$	Concentration of DAMP to activate Kupffer cell	11.5	Estimated
$\phi_{PDGF,migrate}$	Concentration of PDGF to trigger HSC to migrate	1.2	Estimated
$\phi_{TGF\beta,activate}$	Concentration of TGF $\beta$ to activate quiescent HSC	1.0	Estimated
$\phi_{CXCL1,migrate}$	Concentration of CXCL1 to trigger neutrophil to migrate	2.0	Estimated
$\phi_{CCL2,migrate}$	Concentration of CCL2 to trigger infiltrating macrophage to migrate	1.2	Estimated
NA	Fraction of dying Kupffer cells	~5/6	Estimated from Graubardt et al., 2017
$t_{Ly6C^{high} \rightarrow Ly6C^{low}}$	Transforming time from Ly6C-high phenotype to Ly6C-low phenotype for macrophages	~72 hours	Estimated from Zigmond et al., 2014
$t_{elimination}$	Engulfment and elimination duration of macrophages	~3 hours	Estimated from Haecker et al., 2002
$t_{IM,life}$	Lifetime of infiltrating macrophages	~4 days	Estimated from Zigmond et al., 2014
$t_{Neutrophil,life}$	Lifetime of neutrophils	~48 hours	Graudardt et al., 2017

1529 The concentration unit of molecules: 1 equals to 5 ng/ml.

1530 **Table S2. Reference of each arrow in Figure 1B, related to Figure 1.**

Label	Reference	Function	Type	Prob.
1	Li et al., 2020, Calderwood et al., 2016	Injured and dead hepatocytes produce DAMPs	p	1
2	Martin-Murphy et al., 2010	DAMPs activate Kupffer cells	+	1
3	Mihm, 2018	DAMPs activate infiltrating macrophages	+	2
4	Canbay et al., 2003	Kupffer cells engulf dead hepatocytes	-	1
5—7	Pinzani et al., 1994	Platelets, active Kupffer cells and infiltrating macrophages produce PDGF	p	1
8	Melton and Yee, 2007, Yang et al., 2003	PDGF attracts HSCs to migrate	+	1
9	Krenkel et al., 2014	Active Kupffer cells produce CCL2	p	1
10—12	Baeck et al., 2012	Platelets, active HSCs and infiltrating macrophages produce CCL2	p	1
13	Baeck et al., 2012	CCL2 attracts infiltrating macrophages to migrate	+	1
14	Marra and Tacke, 2014	Active Kupffer cells produce CXCL1	p	1
15	Kisseleva and Brenner, 2007	Active HSCs produce CXCL1	p	1
16	Marra and Tacke, 2014	CXCL1 attracts neutrophils to migrate	+	1
17	Marra and Tacke, 2014	Neutrophils induce necrosis of hepatocytes	-	1
18	Imamura et al., 2005	Infiltrating macrophages activate HSCs	+	2
19.a	Tacke and Zimmermann, 2014	Infiltrating macrophages eliminate active HSCs	-	1
19.b	Kisseleva et al., 2012 & Troeger et al., 2012	Infiltrating macrophages revert active HSCs to quiescent phenotype	-	2
20	De Bleser et al., 1997	Active Kupffer cells produce TGF $\beta$	p	1
21	Cai et al., 2018, Imamura et al.,	TGF $\beta$ activates HSCs	+	2

	2005			
22	Boulter et al., 2012	Infiltrating macrophages eliminate dead hepatocytes	-	2
23	Meyer et al., 2015	Platelets promote proliferation of hepatocytes	+	1
24	Seki et al., 2007	Active HSCs attract Kupffer cells to migrate	+	2

1531 Type: “p” indicates production; “+” indicates positive effect; “-” indicates negative effect.

1532 Prob.: “1” indicates highly probable with direct experimental support; “2” indicates probable

1533 with indirect experimental support.